1   **Extracellular Matrix Modulates Outgrowth Dynamics in Ovarian Cancer.**

2   Sarah Alshehri[1]*, Tonja Pavlovič[1]* Sadaf Farsinejad[1], Panteha Behboodi[2], Li Quan[2], Daniel

3   Centeno[1], Douglas Kung[1], Marta Rezler[3], Woo Lee[12], Piotr Jasiński[4], Elżbieta Dziabaszewska[4],

4   Ewa Nowak-Markwitz[5], Dilhan Kalyon[2], Mikołaj P. Zaborowski[5]**, and Marcin Iwanicki[1]**

5   [1] Department of Chemistry and Chemical Biology, Stevens Institute of Technology, Hoboken,

6   USA

7   [2] Department of Chemical Engineering, Stevens Institute of Technology, Hoboken, USA

8   [3] Poznań University of Medical Sciences, Poznań, Poland

9   [4] Department of Pathology, Poznań University of Medical Sciences, Poznań, Poland

10   [5] Department of Gynecology, Obstetrics and Gynecologic Oncology, Division of Gynecologic

11   Oncology, Poznań University of Medical Sciences, Poznań, Poland

12   * These authors contributed equally.

13   ** Correspondence: miwanick@stevens.edu (lead contact) or mzaborowski@ump.edu.pl

14   **Keywords:** ovarian cancer, outgrowths, extracellular matrix, laminin γ1, collagen, tumor

15   microenvironment, ascites

16   **ABSTRACT**

17   Ovarian carcinoma (OC) forms outgrowths that extend from the outer surface of an afflicted

18   organ into the peritoneum. OC outgrowth formation is poorly understood because there is

19   limited availability of OC cell culture models to examine the behavior of cell assemblies that

20   form outgrowths. Prompted by immunochemical evaluation of extracellular matrix (ECM)

21   components, laminin γ1 and collagens, in human tissues representing untreated and

22   chemotherapy-recovered OC, we developed laminin- and collagen-rich ECM-reconstituted cell

23   culture models amenable to studies of cell clusters that can form outgrowths. We demonstrate

24   that ECM promotes outgrowth formation in fallopian tube non-ciliated epithelial cells (FNE)

25   expressing mutant p53-R175H and various OC cell lines. Outgrowths were initiated by cells

26   that had undergone outward translocation and, upon mechanical detachment, could intercalate

27   into mesothelial cell monolayers. Electron microscopy, optical coherence tomography (OCT),

28   and small amplitude oscillatory shear experiments revealed that high ECM concentration

29   increased ECM fibrous network thickness and led to high shear elasticity in the ECM

30   environment. These physical characteristics were associated with the suppression of

31   outgrowths. A culture environment with low ECM concentration mimicked viscoelasticity of

32　malignant peritoneal fluids (ascites) and supported cell proliferation, cell translocation, and

33　outgrowth formation. These results highlight the importance of ECM microenvironments in

34　modulating OC growth and could provide an additional explanation of why primary and

35　recurrent ovarian tumors form outgrowths that protrude into the peritoneal cavity.

36　**INTRODUCTION**

37　Ovarian carcinoma (OC) can arise from the outer mucosa of the epithelial cell surfaces

38　covering the reproductive organs including the endometrium,[1] ovary,[2] and fallopian tubes.[3]

39　Within malignant tissue, transformed epithelial cells can form outgrowths capable of

40　protruding away from the basement membrane and sub-epithelial stroma into the peritoneal

41　cavity.[4] Outgrowths can detach, disseminate within malignant peritoneal fluid (ascites),

42　superficially attach, and intercalate into the mesothelium, contributing to the disease

43　progression.[5,6] The ascites contain ECM molecules[7] and ECM is also enriched within cell-

44　cell junctions of detached tumor outgrowths.[8] Thus, investigating the contribution of ECM to

45　processes associated with OC outgrowth formation would provide invaluable information

46　about the mechanisms of disease progression.

47　ECM is a molecular scaffold that is rich in numerous glycosylated proteins including laminin

48　γ1[9] and collagens[10] which, through interaction with cell surface receptors,[11] provide

49　mechanical[12–15] and biochemical[16,17] cues competent in regulating tissue development[18,19]

50　and malignant progression.[20,21] Recent histologic examination of OC outgrowths protruding

51　from the fallopian tube demonstrates enrichment of laminin γ1 within tumor cells capable of

52　forming outgrowths.[22] Consistent with these findings, it was previously reported[8] that

53　detached human fallopian tube non-ciliated epithelial (FNE) cells expressing various p53

54　mutations deposited ECM molecules supportive of both tumor survival and cell-ECM-cell

55　adhesion. A recent study using second harmonic visualization of outgrowths arising in the

56　fallopian tube revealed the presence of additional ECM components, collagens.[23] Collagen

57　molecules were found to form fibrillar and wavy networks beneath basal surfaces of

58　transformed epithelium. Taken together, these data provoked questions of whether constituents

59　of the tumor microenvironment, such as ECM, regulate the dynamics of outgrowth-forming

60　cell clusters.

61　Reconstitution of cell cultures with Matrigel® (MG), a basement membrane extract rich in both

62　laminin and collagen, has become a standard approach[24] in studying the role of ECM in

63 cellular growth,[25] migration,[26] and death.[27] Recent studies[28–31] employed MG to grow OC
64 cells to evaluate their response to treatments in the context of three-dimensional (3D) spheroid
65 cultures, which resemble malignant tissue organization more closely than two-dimensional
66 (2D) cell cultures. While these studies provided a static view of tumor cells with ECM
67 reconstitution, the contribution of ECM to the dynamic process of OC growth remains
68 unknown.

69 In this report, we have performed immunochemical evaluations of laminin γ1 and collagens in
70 OC representative of disease progression before and after chemotherapy. Similar to OC
71 tumorigenesis from the fallopian tube,[22] we found that laminin γ1 was associated with tumor
72 cells, whereas collagens formed fibrillar networks within the surrounding microenvironment.
73 These studies raised a question of whether ECM deposition within tumor cells and adjacent
74 microenvironment contribute to OC outgrowth dynamics. To address this question, we
75 deployed laminin- and collagen-rich (MG) ECM-reconstituted suspended or adhered cell
76 culture models. To study the dynamics of OC cell clusters, live-cell imaging and quantitative
77 image processing of cell proliferation and translocation were employed. We found that ECM
78 reconstitution of suspended cell clusters induced outgrowths in FNE cells expressing mutant
79 p53-R175H, the cells-of-origin for a significant subset of OCs, as well as other genetically
80 distinct and well-established OC cell lines. Live-cell imaging revealed that outgrowths were
81 initiated by cell clusters that had undergone outward translocation and, upon mechanical
82 detachment, could intercalate into mesothelial cell monolayers – the most frequent physiologic
83 sites of metastasis for OC. Increased ECM concentration altered the thickness of the fibrous
84 network and the viscoelastic characteristics of the microenvironment, which led to the
85 suppression of cell proliferation, directional cell translocation, and formation of outgrowths.
86 Furthermore, ECM-reconstituted cultures that supported outgrowths, cell proliferation, and cell
87 translocation mimicked the viscoelastic properties of peritoneal fluids (ascites).

88 Our results are consistent with a model whereby low-elasticity ECM microenvironments
89 support cell proliferation and translocation of cell clusters that form outgrowths. Our data
90 provide additional explanation of why primary and recurrent OCs favor forming outgrowths
91 that protrude into peritoneal cavity, as opposed to breaching underlying collagen-dense tissues.

92

93

RESULTS

OC tumor outgrowths are associated with distinct ECM deposition.

Detached OC cell clusters deposit ECM on cell surfaces to support survival and cell-ECM- and cell-cell adhesion.[8] Pathologic[4] and genomic[32] examination of tumors indicate that the sources of detached OC cell assemblies are malignant outgrowths that can detach and disseminate into the peritoneal space from the surface of the fallopian tubes, ovaries, and the omentum. To examine whether OC outgrowths are associated with ECM deposition, we used
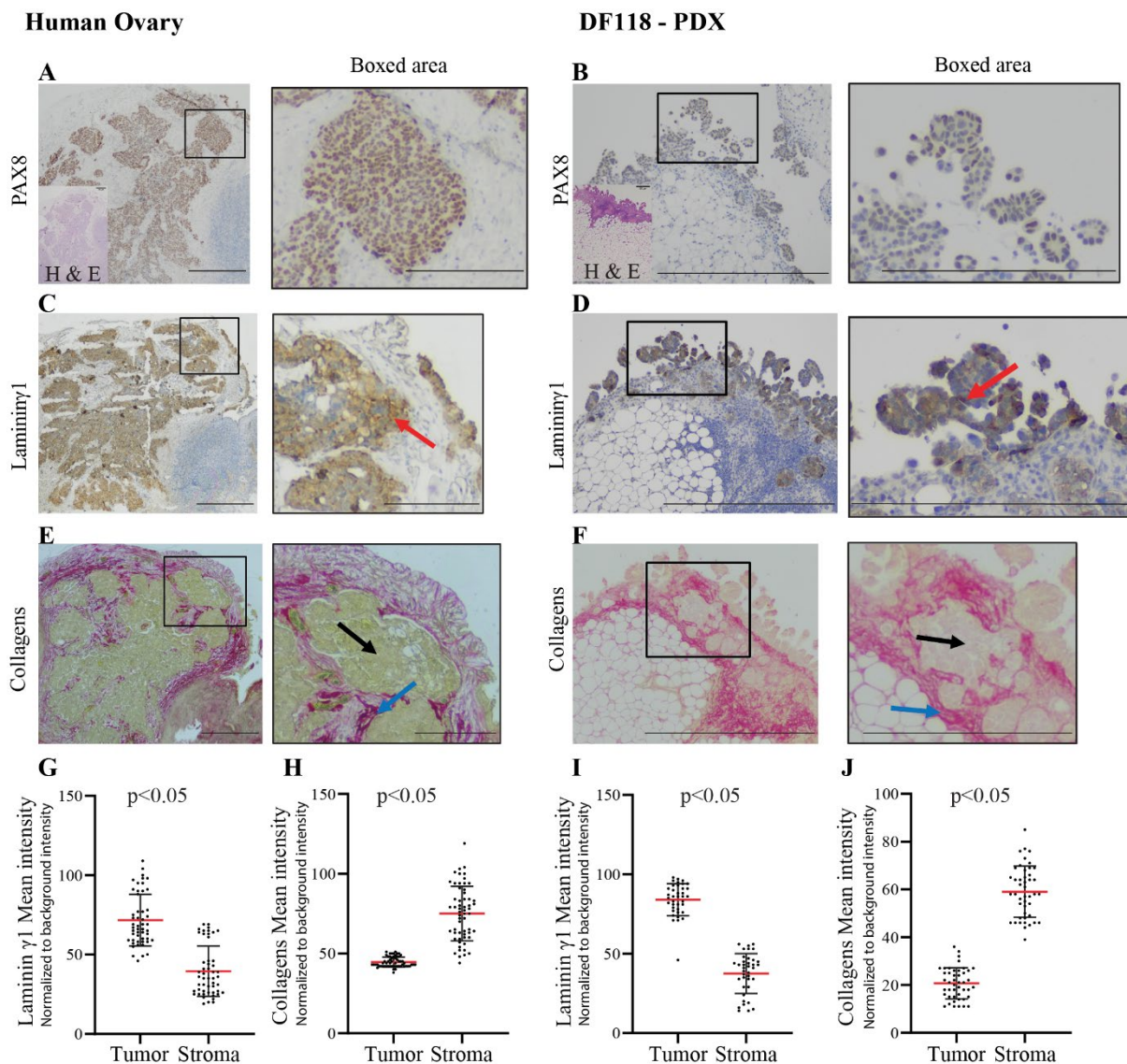

Figure 1. Immuno and chemical evaluation of laminin γ1 and collagen. (**A, B**) PAX8-positive OC outgrowths, and PAX8-negative surrounding connective tissue. Representative images of laminin γ1 (**C, D**), and collagen (**E, F**) expression in tumors protruding from human ovary (**C, E**), or in xenograft experiments, from the surface of the omentum (**D, F**). Red arrows point to the deposition of laminin γ1. Blue arrows indicate fibrillar collagen structures within the tumor's connective tissue, whereas black arrows represent collagen deposition within tumors.

106 Quantification of laminin γ1 (**G, I**) and collagen (**H, J**) expression in PAX8-positive tumor outgrowths and PAX8-
107 negative surrounding tissue. Each data point represents one region of interest (ROI) within tumor outgrowth or
108 surrounding stroma. In each group, G: 51, H: 59, I: 38, and J: 45 ROIs/ condition (tumor and stroma). All data
109 points are shown with bars indicating mean ± SD. An unpaired, two-tailed, non-parametric Mann-Whitney test
110 was used to examine statistical differences between data sets. Intensity values are normalized to background level
111 (area without tissue) after RGB image conversion to 8-bit gray scale (0-255 pixels range).[33] Bars are 100 μm and
112 50 μm in boxed area.

113 combination of immunohistochemistry (IHC) for laminin γ1 and picrosirius red staining for
114 collagen.[34] This approach revealed that cell clusters, which were positive for OC marker
115 PAX8, grew outward from the human ovary surface (**Figure 1A**), or protruded from the surface
116 of the omentum in patient-derived xenograft (PDX) models of OC (**Figure 1B**). These OC
117 outgrowths contained laminin γ1 (**Figure 1C, D**) and, to a much lesser degree, collagens
118 (**Figure 1E, F**). In the same tissue sections, we observed that the adjacent extra-tumoral
119 connective space exhibited low laminin γ1 levels but contained dense fibrillar collagen
120 networks (**Figure 1C-F**). Quantitative image analysis of laminin γ1 and collagen expression
121 revealed differential patterns of localization. Laminin γ1 was enriched within tumors (**Figure
122 1G, I**), whereas collagens were enriched within the extra-tumoral space (**Figure 1H, J**). Taken
123 together, these results demonstrate that OC outgrowths are associated with at least two ECM
124 microenvironment factors, laminin γ1 and collagens.

125 **Laminin γ1 and collagens are associated with OC tumors before and after chemotherapy.**

126 OC patients often develop recurrent disease, which is characterized by the continuous evolution
127 of outgrowths and the presence of detached tumor clusters in the peritoneal cavity.[7] These
128 clinical observations prompted us to examine whether chemotherapy-recovered tumors are
129 associated with laminin γ1 and a collagen-rich ECM microenvironment. ECM deposition was
130 evaluated in PAX8-positive primary tumors in the ovary (**Figure 2A**) and matching omental
131 metastases (**Figure 2B-C**), representing tumors before and after neoadjuvant chemotherapy.
132 Examination of these tissue samples revealed laminin γ1 and collagen deposition before and
133 after chemotherapy (**Figure 2D-E**), suggesting that OC after chemotherapy is associated with
134 the presence of laminin γ1 and collagens. These findings support the idea that laminin and
135 collagen-rich ECM could contribute to outgrowth dynamics of primary and recurrent tumors.
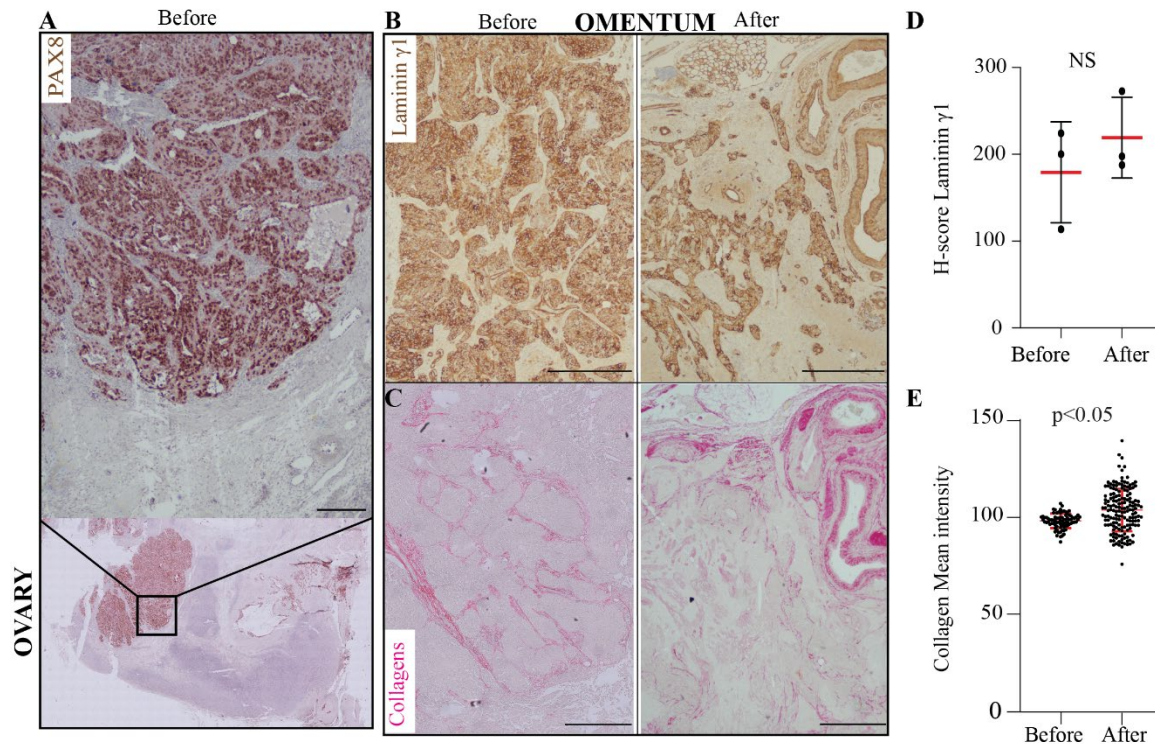
Figure 2. OC before and after chemotherapy is associated with spatially distinct laminin γ1 and collagen ECM microenvironments. (**A**) Hematoxylin and PAX8 stain of high-grade serous ovarian cancer (HGSOC) growing within the ovary before chemotherapy; bar is 100μm. (**B**) Laminin γ1 and (**C**) collagen deposition in matched omental tissue of HGSOC before and after chemotherapy; bar is 500μm. (**D**) H-score quantification of laminin γ1 positivity in matched tissue samples representing HGSOC before and after taxane-platin therapy. Tissues were analyzed from three patients (n=3). Wilcoxon sum rank test was used to compare the difference between the groups, NS= Not-Statistically different. Data points are presented as mean ± SD. (**E**) Quantification of collagen expression in omental metastases before and after chemotherapy. Each data point represents one region of interest (ROI); Before: 82 & After: 160 ROIs. All data points are shown with bars indicating mean ± SD. An unpaired, two-tailed, parametric student t-test with Welch's correction was used to examine statistical differences between data sets. Intensity values are normalized to background level (area without tissue) after RGB image conversion to 8-bit grayscale (0-255 pixels range).[33]

ECM reconstitution in OC spheroids promotes outgrowths.

Laminins (including laminin γ1) and collagens (including collagen IV) represent major scaffolding components of the basement membrane[35–37] and of the reconstituted basement membrane extract, Matrigel® (MG).[37] Thus, to mimic a laminin γ1 and collagen microenvironment associated with OC, we tested whether addition of MG would support formation of OC outgrowths in a suspended spheroid cell culture model. We initially examined effects of MG addition on outgrowth formation in normal fallopian tube non-ciliated epithelial cells expressing mutant p53 R175H (FNE-m-p53). We selected this cell line, because (1) non-ciliated fallopian tube cells, with mutations in the *TP53* gene, are thought to be precursor cells

157 of OC,[3] and (2) we have recently demonstrated, using this cell line, that expression of m-p53

158 in FNE cells induces acquisition of transformed phenotypes associated with OC progression,

159 such as survival of suspended spheroids and mesothelial intercalation.[8] Here, we examined

160 the outgrowth-forming capabilities of FNE-m-p53 or FNE cells transduced with an empty

161 control vector in an OC spheroid model. To obtain OC spheroids, we clustered OC cells in low-

162 adhesion wells and allowed them to grow in suspension for 24 hours (**Figure 3A**). To mimic

163 the laminin and collagen rich ECM microenvironment, we then embedded the OC spheroids in

164 media containing 2% MG (**Figure 3A**). This ECM reconstitution condition of 2% MG was

165 selected based on previous reports that 2% MG supported the growth of breast and ovarian

166 spheroid cultures plated on MG layers covering flat culture surfaces.[27] Live-cell microscopy

167 revealed that FNE-m-p53, but not wild-type FNE, significantly expanded and formed

168 outgrowths – cell assemblies that, over time, began to extend beyond the main spheroid

169 structure (**Figure 3B-C, and MOVIE 1**). We observed that FNE-m-p53 spheroids in 2% MG

170 formed outgrowths with an average frequency of 30%, whereas no outgrowths were detected

171 in spheroids composed of control FNE cells in 2% MG, or FNE-m-p53 spheroids lacking MG
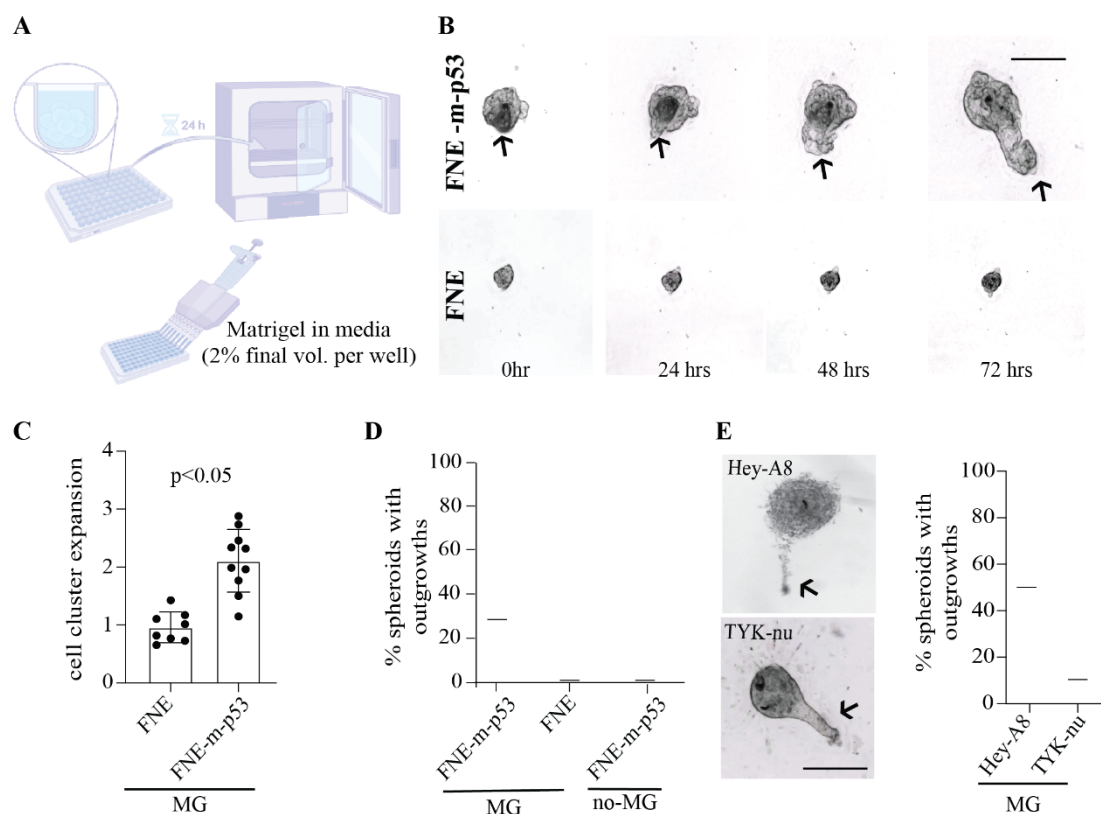
172 **Figure 3.** Laminin- and collagen-rich ECM reconstitution stimulates outgrowths in suspended cultures of various

173 OC cells. (**A**) Graphical representation of the assay design to study outgrowth dynamics. (**B**) Representative

174 bright-field images of outgrowth formation in FNE cells expressing plasmid containing m-p53R175H (FNE-m-

175 p53), or control plasmid, and cultured as suspended clusters reconstituted with 2% MG. Cell structures were

176 cultured for 7 days before imaging and subsequently followed for an additional 72 hrs. (**C**) Quantification of 3D

177 structure (spheroid) expansion, where each dot represents fold change in area, over 72 hrs of filming time, in a
178 spheroid. Total spheroids: 8 for FNE & 10 for FNE-m-p53. All data points are shown with bars indicating mean
179 ± SD. An unpaired, two-tailed, parametric student t-test with Welch's correction was used to examine statistical
180 differences between data sets. (**D**) Quantification of cell clusters with outgrowths in FNE-m-p53 or FNE cells.
181 Bar represents an average percentage of outgrowth formation with at least 30 cell clusters analyzed. (**E**)
182 Representative bright-field images of outgrowths in Hey-A8 and TYK-nu ovarian cancer cell lines, and
183 quantification of outgrowths in Hey-A8 or TYK-nu. Bars represent an average percentage of outgrowth formation
184 in three independent experiments with 20-30 spheroids scored per experiment. Scale bars are 200 μm.

185 embedding (**Figure 3D**). These data are consistent with the implicated role of ECM deposition
186 in supporting outgrowth development (**Figure 1 and Figure 2**).

187 Intraperitoneal dissemination is a common feature among different subtypes of OC, including
188 serous and non-serous subtypes.[6] We therefore wanted to evaluate whether multiple OC cell
189 lines, representing a diverse variety of OC subtypes, can form similar outgrowths when
190 cultured as suspended spheroids embedded in 2% MG. We examined OC cell lines Hey-A8
191 and TYK-nu, representing non-serous and likely serous OC models, as defined by Domcke et
192 al.[38] Similar to FNE-m-p53 spheroids, reconstitution of Hey-A8 (**MOVIE 2**) or TYK-nu
193 (**MOVIE 3**) spheroids with 2% MG prompted outgrowth formation (**Figure 3E**). The average
194 percentage of outgrowth formation among Hey-A8 and TYK-nu spheroids varied from 50% to
195 10%, respectively (**Figure 3E**). Outgrowth formation in spheroids observed in different OC
196 cell lines, but not normal FNE cells, suggests that ECM collaborates with transformation to
197 support outgrowths.

198 **Detached outgrowths clear mesothelial monolayers**.

199 OC outgrowths can ultimately detach from the transformed tissue, transit into the fluids of the
200 abdominal cavity, and intercalate into mesothelial surfaces of other abdominal organs, such as
201 the omentum.[1] To assess whether OC outgrowths, evoked by ECM reconstitution, possess the
202 ability to intercalate into mesothelial cell layers, we utilized Hey-A8 spheroids embedded in
203 2% MG due to their tendency to form long protruding outgrowths that are amenable to
204 dissociation under a dissecting microscope. We mechanically separated Hey-A8 outgrowths
205 from the spheroid structure and co-cultured both entities on top of a mesothelial cell monolayer
206 expressing green fluorescent protein (GFP) (**Figure 4A**). To examine the ability of spheroids
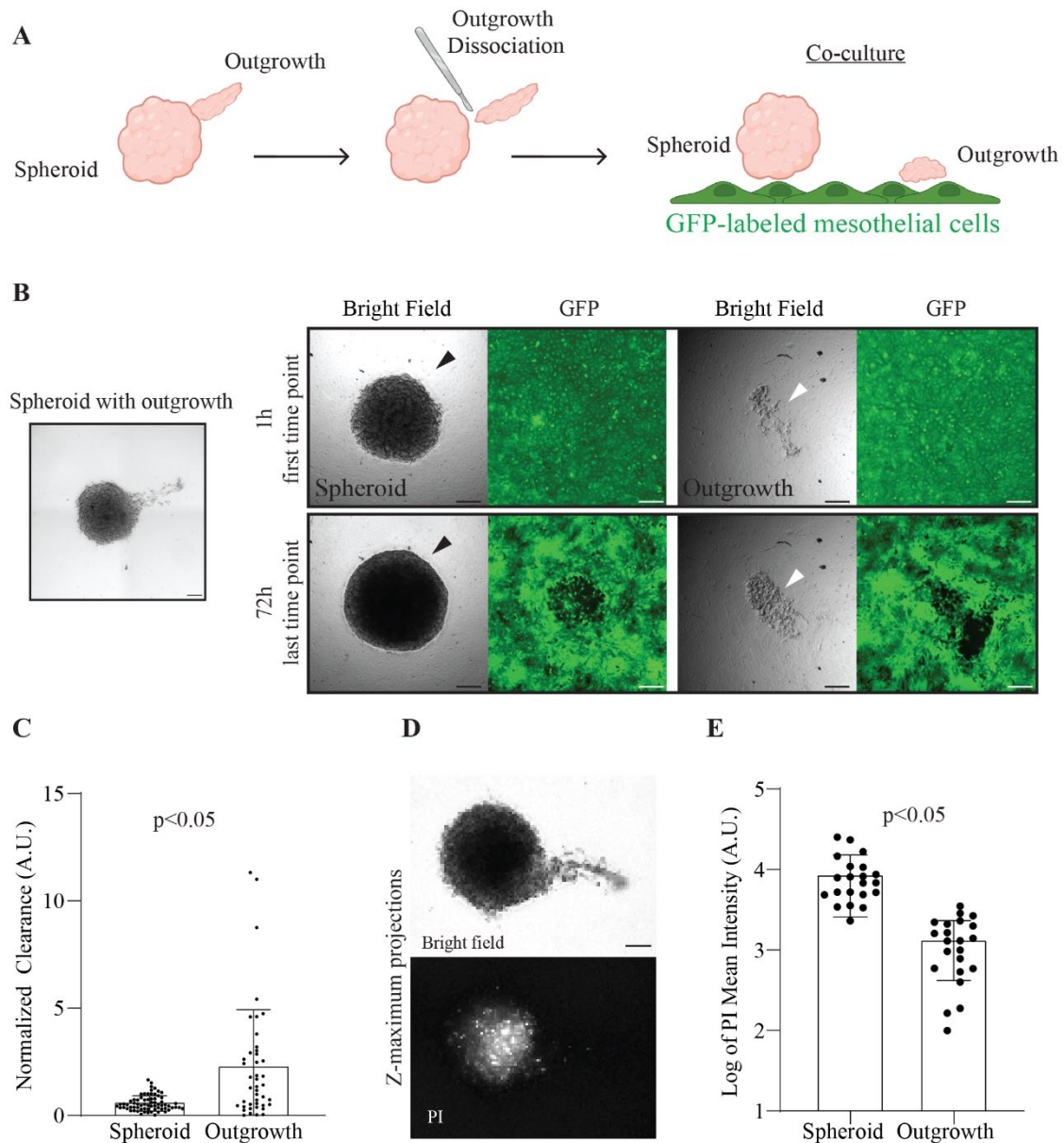
Figure 4. Detached outgrowths clear mesothelial monolayers. (**A**) Schematic representation of Hey-A8 outgrowth detachment and co-culture with mesothelial cells expressing GFP. Created with BioRender.com. (**B**) Representative bright-field image of a spheroid before outgrowth detachment, followed by representative bright-field and fluorescent images of mesothelial clearance by Hey-A8 spheroid (black arrow) or detached outgrowth (white arrows); scale bar is 200 μm. (**C**) Quantification of mesothelial clearance by Hey-A8 spheroids and detached outgrowths.[39] Each data point represents a spheroid or outgrowth from two independent experiments from 69 spheroids and 43 outgrowths. (**D**) Representative bright-field and corresponding fluorescent maximum projection images of a Hey-A8 spheroid forming an outgrowth and treated with propidium iodide (PI) to spatially visualize cell death within the structure; scale bar is 200 μm. (**E**) Quantification of PI incorporation by spheroids or outgrowths. Twenty-one Hey-A8 cell structures were analyzed. In C and E all data points are shown with bars indicating mean ± SD, and an unpaired, two-tailed, non-parametric, Mann-Whitney test was used to examine statistical differences between data sets.

219   and their corresponding outgrowths to invade mesothelial cell layers, we used a well-

220   established mesothelial clearance assay,[40] which relies on measuring the area where initially

221   adherent mesothelial cells are displaced by the introduction of OC spheroids.[39]

222   The formation of the cleared area is visualized by the time-dependent exclusion of GFP

223   fluorescence, which is representative of mesothelial cell displacement from beneath the

224   intercalating OC spheroid. Using this displacement assay, we were able to observe that

225   detached outgrowths induced more mesothelial cell clearance compared to their corresponding

226   OC spheroid clusters (**Figure 4B-C**). This observation could be due to spatial variation in

227   viability between OC cells located within the outgrowth and cells within the spheroid. Spatial

228   examination of cell viability using propidium iodide (PI), a fluorescent dye permeable only to

229   dead cells, revealed a greater quantity of dead cells localized to the core of the OC spheroids

230   relative to the outgrowths, which demonstrated minimal PI incorporation and thus increased

231   cell viability (**Figure 4D-E**). These observations are consistent with the hypothesis that OC

232   cell assemblies capable of forming outgrowths are viable and can efficiently intercalate into

233   mesothelial cell layers upon detachment.

234   **Increased ECM inhibits formation of outgrowths.**

235   As we have so far observed that ECM reconstitution of OC spheroids was able to induce

236   formation of cell outgrowths that were able to intercalate into mesothelial cell layers, we

237   wanted to further investigate the role of ECM in the regulation of OC cell outgrowths.

238   Motivated by our initial observation indicating that OC prefers to grow away from collagen

239   dense areas (**Figure 1**), we examined whether manipulation of ECM concentrations affect

240   outgrowth formation. We compared the outgrowth formation capability of FNE-m-p53 and

241   Hey-A8 spheroids reconstituted with 2% or 25% MG. As expected, reconstitution of both cell

242   types with 2% MG induced outgrowth formations. In contrast, 25% MG culturing conditions

243   significantly attenuated the development of outgrowths (**Figure 5A-B**), indicating that

244   increasing ECM concentrations can suppress outgrowths. In addition, we observed that under

245   25% MG conditions, both FNE-m-p53 and Hey-A8 spheroids appeared to be significantly

246   smaller when compared to 2% MG reconstitution conditions (**S. Figure 1A-B**). In comparison

247   to FNE-m-p53 spheroids, Hey-A8 spheroids cultured in 25% MG also appeared to be less

248   compacted, coarse, and more disorganized (**Figure 5B, inset**). This may suggest that elevating

249   ECM concentrations can have divergent effects on different OC cell lines. In the case of Hey-

250   A8 spheroids, increased concentrations of ECM may have disrupted cell-cell adhesions, as

251   suggested by the decrease in N-cadherin staining at the edge of the spheroids (**S. Figure 2**).

252   Decrease in spheroid size due to an increase in ECM concentrations indicated the possibility

253   that increasing ECM deposition could affect cell proliferation.
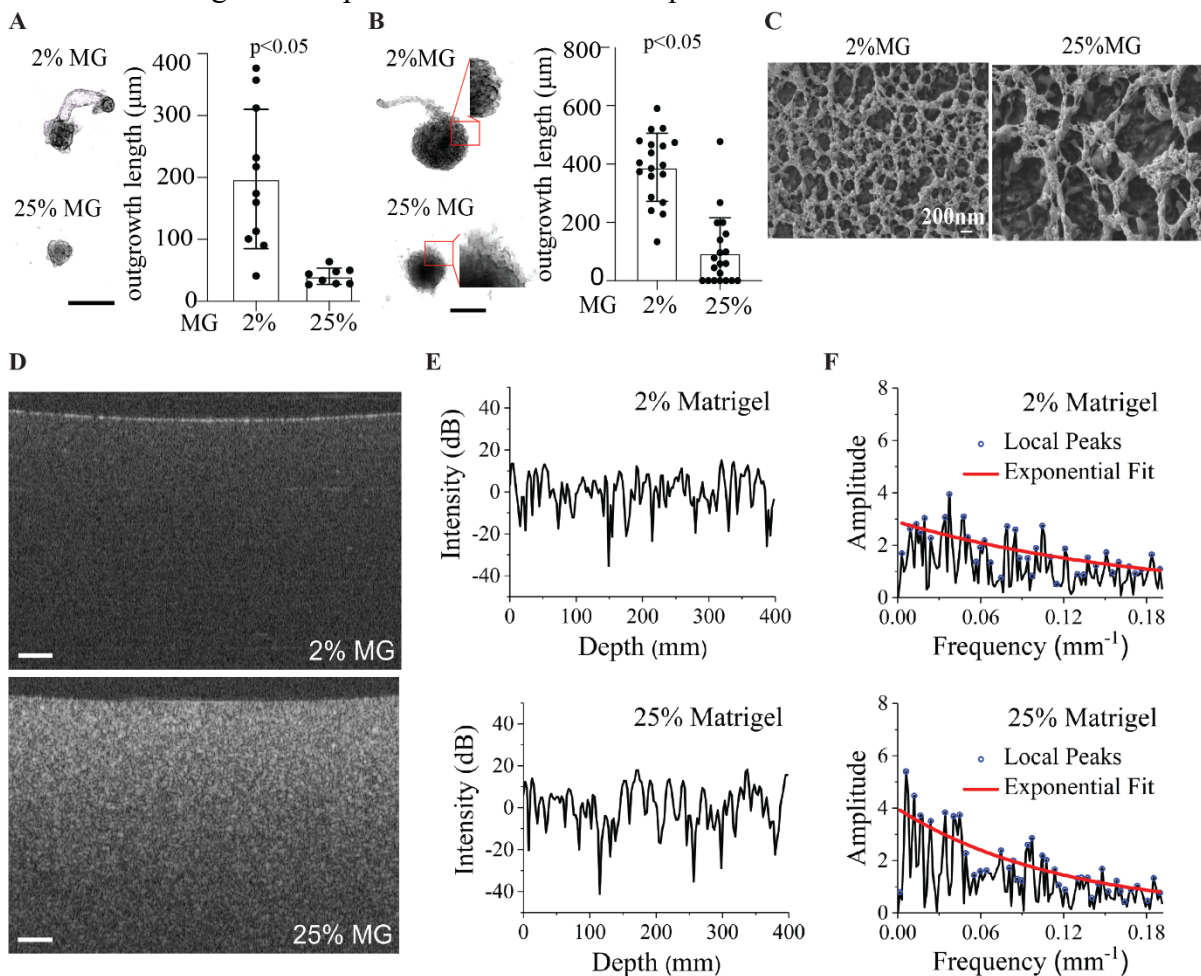
Figure 5. Elevation of ECM concentration inhibits outgrowths. Representative bright-field maximum Z-projection images of (**A**) FNE-m-p53 spheroids reconstituted with 2% or 25% MG; scale bar is 250 μm. (**B**) Hey-A8 spheroids reconstituted with 2% or 25% MG; scale bar is 500 μm. Spheroids were grown for 10 days, and the images show the final time point. Dot plots represent the distribution of outgrowth lengths from individual spheroids reconstituted with 2% or 25% MG. All data are shown with bars indicating mean ± SD. An unpaired, two-tailed, parametric student t-test with Welch's correction was used to examine statistical differences between data sets. (**C**) Representative electron scanning micrographs representing 2% and 25% MG. (**D**) Representative OCT B-scan images of 2% and 25% MG; scale bars are 100 μm. (**E**) Representative OCT depth-resolved intensity profiles where the slopes from optical attenuation are removed. (**F**) Amplitude spectra of the spatial frequency corresponding to the panel -E- show relatively stronger low-frequency components from 25% MG, and exponential fit of local peaks indicating a faster decay rate in 25% MG.

265   To explore this possibility, we took advantage of a 2D cell culture assay in which the cell

266   monolayer is overlaid with MG,[41] thereby partially mimicking conditions of ECM

267   encapsulation (**S. Figure 3A**). We integrated this assay with live-cell imaging of FNE-m-p53

268   and Hey-A8 cells stably expressing GFP or monomeric Kusabira-Orange2 (mKO2),

269   respectively. FNE-m-p53-GFP or Hey-A8-mKO2 cells cultured with 25% MG significantly

270   decreased cell proliferation (**S. Figure 3B-C, MOVIE 4 and 5**). These results were

271   additionally supported by data indicating that 25% MG reconstitution of Hey-A8 spheroids

272   significantly reduced the number of cells undergoing active DNA replication, as assessed by

273   the 5-ethynyl-2'-deoxyuridine (EdU) incorporation assay (**S. Figure 3D**). We selected Hey-A8

274   spheroids to examine EdU incorporation due to the formation of significantly larger spheroid

275   structures when compared to FNE-m-p53 cells (**S. Figure 1A-B**), enabling robust EdU

276   incorporation analysis. Taken together, these results suggest that ECM play a significant role

277   in the OC cell environment and can modulate OC cell proliferation and outgrowth formation.

278   **Increased ECM leads to the formation of thick fibrillar networks.**

279   The phenotypic influence of ECM concentrations on outgrowth formation and cell proliferation

280   (**Figure 5A-B, and S. Figure 3**), combined with the previous IHC examination of tumors,

281   which indicate that OC tumors can form protruding outgrowths away from thick collagen

282   fibrous network associated with tumor-surrounding tissue (**Figure 1**), motivated us to examine

283   whether higher ECM concentrations exhibit differences in fibrous network thickness. Scanning

284   electron microscopy (SEM) of MG revealed qualitative differences between ECM networks

285   formed in 2% and 25% MG (**Figure 5C**); network fibers formed in 25% MG appeared to be

286   thicker and more spaced out (larger spaces between fibers) as compared to network fibers

287   formed in 2% MG. For quantitative evaluation of ECM fibers, we imaged the MG samples

288   using optical coherence tomography (OCT), where the endogenous optical contrast describes

289   the microstructure of the sample. The OCT B-scan images revealed a higher contrast from the

290   ECM contents with larger high-intensity clusters in the 25% MG condition compared with the

291   2% MG condition (**Figure 5D**). Also, the representative OCT depth-resolved intensity profiles

292   where the slopes from optical attenuation are removed, show a larger spatial period of intensity

293   fluctuations in the 25% MG (**Figure 5E**), which can be clearly seen with relatively more low-

294   frequency components from the corresponding amplitude spectra (**Figure 5F**). This feature in

295   the spatial frequency was quantified with the decay coefficient from an exponential fit of the

296   local peaks in the amplitude spectra (**Figure 5F**), where a higher exponential decay coefficient

297   in 25% MG indicates relatively stronger low-frequency components, suggesting thicker ECM

298   fibers and/or larger space between ECM fibers in 25% MG.

299

ECM modulates viscoelasticity of OC culture microenvironments.

Based on data demonstrating formation of thicker, spatially distributed – ECM fiber networks in 25% MG cultures, and previous reports indicating positive correlation between MG concentration and elasticity,[42] we wondered whether increasing the concentration of ECM in our model would affect the cell culture's viscoelasticity e.g., changes to time dependent elasticity and the viscous behavior of MG in the cell culture.[43] We characterized the linear viscoelastic material functions of cell culture media containing 2% or 25% MG. This analysis revealed that in culture media supplemented with 25% MG, the loss modulus (G") values representing viscous behavior, which are indicative of the energy dissipated as heat when the culture media is deformed under small-amplitude oscillatory shearing, were within a narrow range of 0.5 to 0.9 Pa in the frequency range of 0.1 to 10 s^{-1}. The loss modulus values were thus not sensitive to the frequency of rotation (**Figure 6A**). Under similar conditions, the storage modulus (G') values representing elasticity i.e., indicative of the energy stored as elastic energy during the deformation of the culture media, were within the range of 3.5 to 4.5 Pa. The storage modulus (G') values were also insensitive to the frequency of rotation (**Figure 6A**).

The loss modulus (G") values of samples cultured in 2% MG ranged between 0.05 to 0.1 Pa while the storage modulus (G') values were between 0.09 to 0.3 Pa (Figure 6C). The storage moduli of 25% MG reconstituted culture media were significantly higher than the loss moduli (G' > G"), and the ratio of G''/G' (tan δ) was below 1 (Figure 6B). On the other hand, the 2% MG reconstitution condition produced tan δ values greater than 1 (Figure 6D), indicating a less elastic nature of the 2% versus the 25% MG. As expected, these results suggest that the elasticity of media containing 25% MG is significantly higher than that containing 2% MG. Measurements of loss and storage moduli of ascites isolated from three different OC patients exhibited a closer similarity to the values of G", G' and tan δ observed in the 2% MG reconstitution condition (Figure 6E-F and S. Figure 4B-C), indicating that ascites may mechanically appear as gels with lower elasticity. Although the study of ascitic viscoelasticity was limited to 3 patient samples that showed considerable G' and G'' variation (S. Figure 4B-C), all the samples exhibited a relatively low storage modulus when compared to 25% MG. Behavior of ascites as weak gels with low torque values could also account for the variability, because data points associated with very low rotation frequencies might be close to the limits

331   the instrument's sensitivity. Nevertheless, the similarity of viscoelastic properties between 2%

332   MG and patient-derived ascites motivated us to evaluate whether ascites possess the ability to
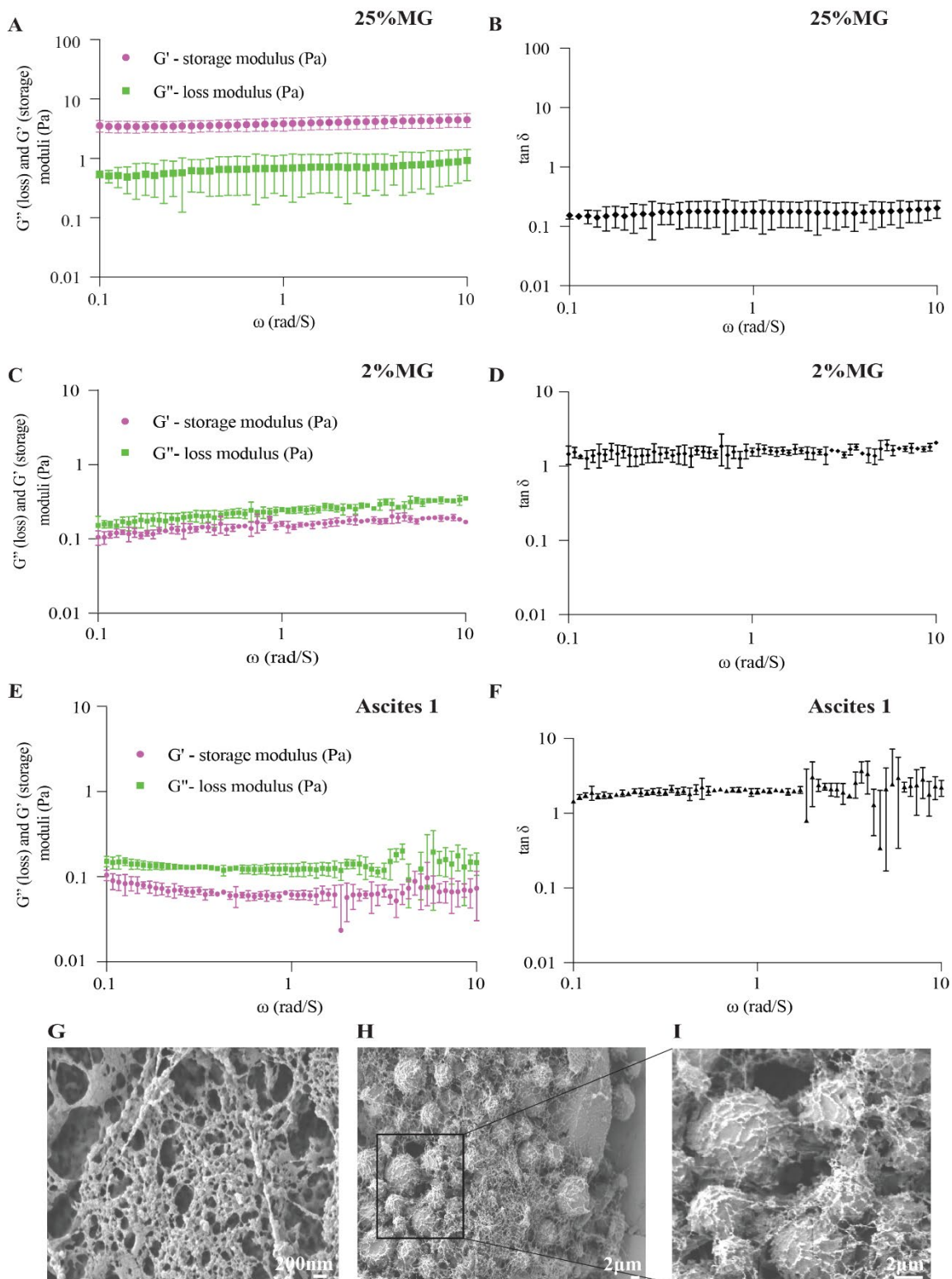
333   **Figure 6**. ECM modulates viscoelastic properties in the OC culture microenvironment. Measurements of storage

334   (elastic) and loss (viscous) moduli in OC cell culture media reconstituted with 2% or 25% of MG (**A, C**); or in

335   ascites isolated from OC patients with a relapsed disease (**E**). (**B, D, F**) Graphs represent calculated tan δ from

336   values reported in A, C & E. (**G, H, I**) Scanning electron micrographs represent the ascitic fibrous network

337 surrounding tumor cells. Each data point represents the mean and SD from triplicate measurements with a total of
338 41 (25% MG), 91 (2% MG) & 91 (ascites) measurements.

339 form extracellular fibrous networks. Scanning electron microscopy of ascitic fluid indicated
340 the presence of structures resembling extracellular fiber networks (Figure 6G). Additionally,
341 fibrous structures were associated with cells that were isolated along with ascites. Moreover,
342 we have detected, using IHC, laminin and collagen fiber-like structures that were associated
343 with detached OC clusters isolated from human or mouse ascites (**S. Figure 5**). Taken together,
344 these results are consistent with the hypothesis that ECM microenvironments with low shear
345 viscosity and elasticity, support OC outgrowth formation.

346 **Increased ECM suppresses directional translocation.**

347 Based on observations that outgrowths are initiated by cell assemblies that translocate outside
348 the main spheroid structure (**Figure 3, MOVIE 1, 2, and 3**), and that increasing ECM
349 concentration suppresses the formation of outgrowths, decreases spheroid size, and impedes
350 cell proliferation (**Figure 5A-B, and S. Figures 1 and 3**), we hypothesized that high ECM
351 concentrations also suppress cell translocation.

352 To track the movement of cells embedded in ECM, we overlaid FNE-m-p53-GFP and Hey-
353 A8-mKO2 cells grown on a 2D surface with media containing 2% or 25% MG (**S. Figure 3A**).
354 We analyzed the cell translocation dynamics of FNE-m-p53-GFP and Hey-A8-mKO2 cells
355 overlaid with differing MG concentrations using an ImageJ-integrated plugin, TrackMate and
356 measured the confinement ratio output, which represents the efficiency of cell translocation
357 away from its original starting point (**Figure 7A**; see Materials and Methods for details). We
358 observed that overlaying FNE-m-p53-GFP or Hey-A8-mKO2 cells with 2% MG resulted in a
359 confinement ratio that was significantly larger than the confinement ratio of cells overlaid with
360 25% MG, indicating more efficient cell translocation (**Figure 7B-E**). Cell tracks appeared more
361 persistent and directional in cells overlaid with 2% MG medium as compared to 25% MG
362 medium (**Figure 7B, D, and MOVIE 6 and 7**), suggesting that an increase in ECM deposition
363 can suppress directional cell translocation and is competent in anchoring cells to their starting
364 point, as supported by the increased number of focal adhesions under 25%MG conditions (**S.
365 Figure 6 and S. Figure 7**). Furthermore, we observed that OC cells superficially attached to
366 the outer surface of murine small intestine did not invade beyond smooth muscle actin positive

367 stroma (**S. Figure 8**), supporting that some OC tumors can grow superficially and do not

368 penetrate beyond stroma and dense ECM.
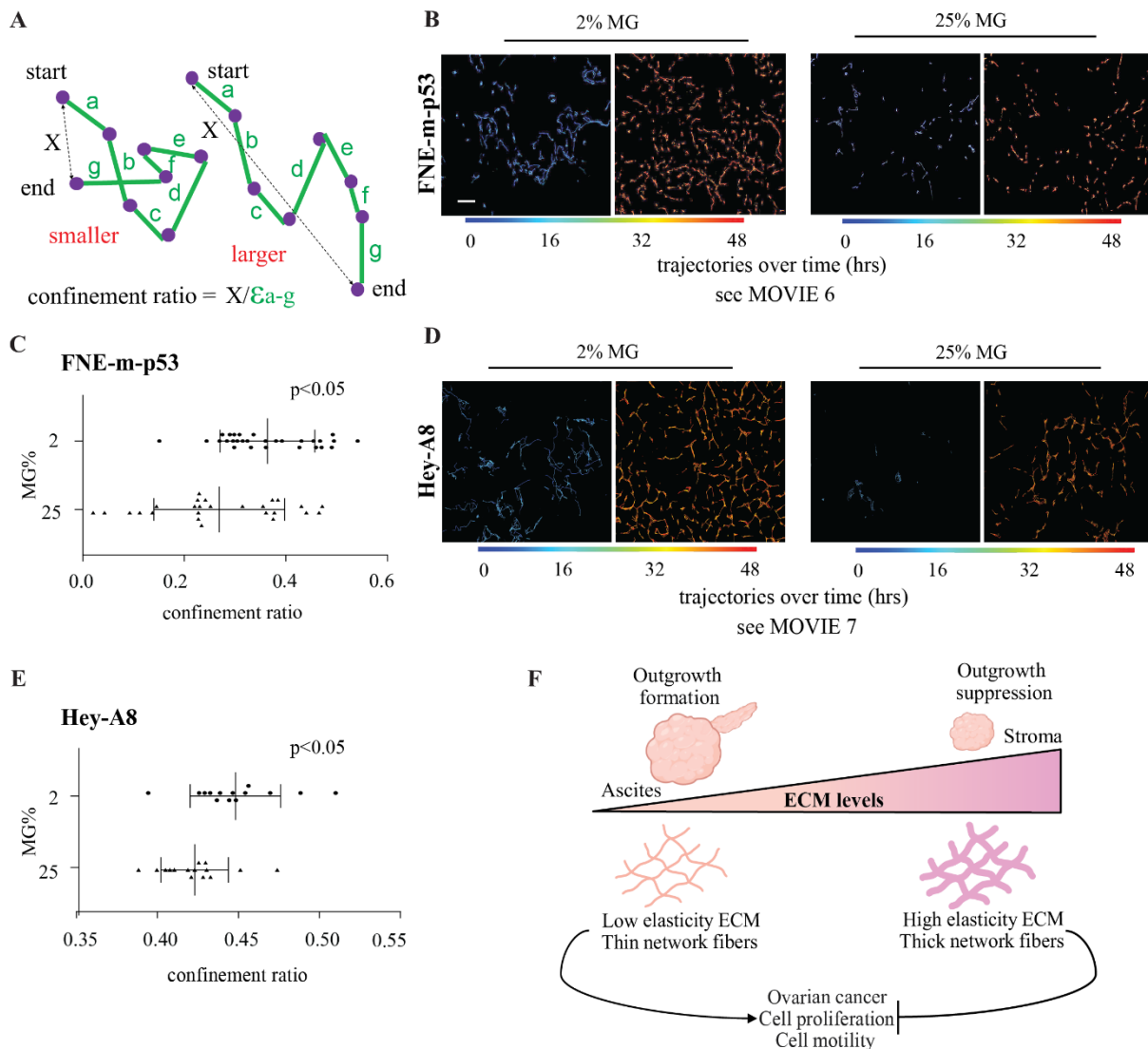
Figure 7. Elevation of ECM concentration suppresses directional cell translocation. (**A**) Graphical illustration of confinement ratio quantification. (**B**) Representative trajectory images of cell translocation within FNE-m-p53 or (**D**) Hey-A8 cell monolayers overlayed with 2% or 25% MG. Each line represents a single cell trajectory formed during 50 frames/time interval. Time zero corresponds to the first 50 frames; scale bar 100 μm. Distribution of confinement ratio within (**C**) FNE-m-p53 or (**E**) Hey-A8 cell monolayers overlayed with various concentrations of MG. Each dot represents one field of view that contained 20-100 cells/ condition (2% vs. 25% MG). All data points are shown with bars indicating mean ± SD. Two independent experiments were performed with a total of 12-30 fields of view. An unpaired, two-tailed, parametric student t-test with Welch's correction was used to examine statistical differences between data sets. (**F**) Graphical representation of key findings in this study. Created with BioRender.com

380 **DISCUSSION**

381 The mechanism of OC dissemination is still poorly understood; it involves the localized
382 spreading of OC cell clusters that grow outward and detach from the primary tumor and
383 disseminate within the peritoneal cavity. To investigate the conditions that prompt the
384 formation of these OC outgrowths, we employed immunohistochemical stains to evaluate
385 tissue samples representing human and PDX models of OC tumors. Immune and histochemical
386 examination of laminin γ1 and collagens revealed that OC outgrowths were identifiable with a
387 distinct ECM microenvironment. The ECM microenvironment observed among carcinoma
388 cells contained abundant laminin γ1 along with lower levels of collagens expression. In
389 contrast, the underlying extra-tumoral stroma exhibited lower laminin γ1 levels but contained
390 dense collagen fibers. We also observed that OC outgrowths were primarily clustered away
391 from the underlying extra-tumoral stroma, towards what we presumed was a less constrictive
392 microenvironment. These results prompted us to use laminin- and collagen-reconstituted 3D
393 tissue culture approaches to discern the conditions promoting the formation of OC outgrowths.

394 Laminin- and collagen-rich MG[37] reconstitution of 2D and 3D OC cell cultures was used in
395 combination with live-cell imaging, SEM, OCT, and rheology to examine the contribution of
396 ECM to OC outgrowth dynamics. Live-cell imaging demonstrated that ECM reconstitution of
397 OC spheroids, representing various OC subtypes, promoted the formation of outgrowths that,
398 upon detachment, exhibited the ability to intercalate into mesothelial cell layers. We observed
399 outgrowth formation in various genetically distinct OC cell lines including FNE-m-p53. ECM
400 reconstitution did not promote the formation of outgrowths in normal, non-transformed FNE
401 cultures, indicating that outgrowth formation is associated with transformed phenotypes of the
402 cells of origin. OC outgrowths were observed to be initiated by cell assemblies that undergo
403 outward translocation[1] from the main spheroid. Increasing ECM concentrations led to
404 increased elasticity of OC cell culture media, suppressed proliferation, decreased directional
405 cell translocation, and suppressed outgrowths. Based on these results we propose a model in
406 which OC cells favor a low elasticity ECM microenvironment to divide, translocate and form
407 outgrowths with the potential to extend into the peritoneal cavity (**Figure 7F**). Our findings
408 could provide reasoning for why some genetically distinct OC subtypes are superficially
409 invasive and prefer to grow away from the ECM-dense stroma and tend to form outgrowth
410 protrusions extending into a more fluid environment such as peritoneal ascites.

411 Recent IHC evaluation of OC within the fallopian tube revealed enrichment of laminin γ1
412 chain,[22] a component of the heterotrimeric laminin αβγ molecule.[44] Consistent with this
413 study, we found that tumor cells representing OC outgrowths protruding from the ovary and
414 omental metastases were enriched in laminin γ1. In contrast to tumor cells, the adjacent stroma
415 displayed low levels of laminin γ1 deposition, highlighting an involvement of γ1-chain
416 containing laminins in the regulation of cell-cell and cell-ECM[2] adhesion among tumor cell
417 assemblies competent in forming outgrowths. Laminins promote the formation of the basement
418 membranes that support epithelial cell proliferation and collective cell migration during tissue
419 development.[45,46] We speculate that formation of a sufficient number of cell-ECM adhesions
420 among OC cells could contribute to tumor expansion and cell translocation, leading to the
421 initiation of the observed outgrowths. In concurrence, our ECM-reconstituted OC spheroid
422 model demonstrated that low concentrations of ECM were conducive in the promotion of
423 cellular proliferation, directional cell translocation and outgrowth formation, while increased
424 ECM concentrations were instead suppressive of the listed phenotypes. We speculate that the
425 latter phenomenon may be attributed to increasing cell-ECM adhesion beyond the optimal
426 point required for the processes.

427 Combination of SEM and OCT imaging revealed that elevation of ECM concentration, in
428 culture, led to the formation of more thick and spaced-out protein fibers. These structural
429 changes in ECM networks were associated with suppression of OC cell proliferation and
430 directional translocation. These results are consistent with previous studies demonstrating
431 collagen-fiber localization beneath OC outgrowths originating from the fallopian tube[23] and
432 within the stroma surrounding metastatic omental implants.[47] Collagen fiber formation occurs
433 when collagen concentration increases,[48] indicating that extra-tumoral fibrils reflect the
434 presence of highly elastic ECM. In addition to negative regulation of cell motion by elevation
435 of collagen fiber content and fiber alignment,[49] increasing diameter of collagen fibers[50] and
436 spacing between collagen networks[51] has been shown to suppress cell motility. These data
437 suggest that not only ECM concentration[51] but also architecture of ECM is important in the
438 regulation of cell motion.

439 Metastatic OC tumor cells superficially invade the mesothelial cell layer of the peritoneal
440 membrane,[6] and we have consistently observed that OC tumors growing within mouse
441 peritoneum colonized surfaces of the omentum or small intestine and formed superficial
442 outgrowths extending into the peritoneal cavity, with minimal invasion of the underlying

443   stroma. Combined with our observations of outgrowth formation under low- but not high- ECM

444   conditions, we suggest that the dynamic evolution of OC outgrowths is supported by low ECM

445   concentration microenvironments (**Figure 3**). OC cell proliferation, translocation, and

446   outgrowth formation were more robust under 2% MG culture conditions, indicating a

447   possibility that elevated levels of ECM surrounding OC spheroids could provide a physical

448   barrier that suppresses the formation of outgrowths and concomitantly hinders dissemination

449   of OC tumor cells into the peritoneal cavity.

450   Recent studies have demonstrated that increasing the concentration of collagen managed to

451   restrict single-cell translocation from cell clusters, as measured by the mean square

452   displacement of the tracked trajectories.[52] Additionally, targeting fibroblasts that produce

453   collagens resulted in reduced collagen deposition and increased OC cluster dispersal.[47]

454   Furthermore, 2D studies of the effects of ECM concentration on cell motility have pointed to

455   the existence of optimal ECM concentrations that support efficient directional cell

456   migration.[53] Concentrations below or above optimal levels did not stimulate fibroblast

457   migration to the same extent.[53] In agreement, our study supports this correlation by

458   demonstrating that OC cells reconstituted with a higher concentration of ECM show a reduction

459   in both directional cell translocation and outgrowth formation. This could be potentially

460   explained by optimal integrin-complex turnover rates under appropriate ECM concentrations.

461   Previously, it has been shown that high concentrations of ECM can lead to strong adhesion,[53]

462   as well as low adhesion turnover.[54] Therefore, we speculate that an OC microenvironment

463   with low ECM concentration supports the formation of adhesion complexes that are more

464   dynamic and, thus, capable of promoting directional cell translocation. In contrast, the strong

465   attachment of OC cells for instance due to presence of thick ECM fibers would lead to static

466   adhesion that could impede directional cell translocation. This speculation is supported by the

467   observation that embedding cell monolayers in high ECM increased the number of paxillin-

468   rich focal adhesions (**S. Figure 6 and 7**).

469   Varying ECM concentrations were observed to modulate viscoelastic characteristics of the

470   microenvironment and could possibly affect cell behavior,[55] including the acquisition of

471   transformed phenotypes in normal cells.[56] Using rheometric analysis of our ECM-

472   reconstituted culture media, we demonstrated that the addition of 2% MG resulted in lower

473   elasticity as compared to the addition of 25% MG, which led to the development of thick

474   fibrous networks and the highly elastic properties of the ECM reconstituted culture media,

475 which is characteristic of a more solid environment (**Figure 6**). Our data demonstrated that
476 ECM concentrations corresponding to lower elastic properties were conducive to cell
477 proliferation, directional cell translocation, and formation of outgrowths. Thus, it may be
478 conceivable to propose that ECM deposited on the surface of primary OC tumor cells creates
479 a low-elasticity ECM microenvironment that provides optimal adhesion and traction force to
480 support cell proliferation and motility of OC tumor cells. In contrast, increasing the deposition
481 of ECM within the OC tumor microenvironment would increase adhesion and suppress cell
482 proliferation, cell translocation, and outgrowth formation (**Figure 7F**). Our model is consistent
483 with clinical observations that OC peritoneal dissemination is associated with tumor
484 outgrowths that protrude from the tumor into the peritoneal cavity[4,22] through ascites [7,57],
485 which likely represent a low-elasticity microenvironment;[7,55] this is supported by
486 measurements of shear moduli values of ascites, resembling those of 2% MG cultures, as well
487 as SEM and IHC images showing fibrous networks overlaying OC cells (**S. Figure 5 and**
488 **Figure 6E-I**).

489 OC outgrowths continue to evolve after chemotherapy because detached OC cell clusters are
490 present within the ascitic fluid and peritoneal cavity of patients with recurrent disease.[7] OC
491 cells that have recovered from chemotherapy may be in direct contact with ECM deposited
492 within tumors and extra-tumoral space (**Figure 2B-E**). Thus, the ECM-reconstitution model of
493 OC outgrowths offers a clinically relevant approach to examining the dynamic processes of
494 disease progression and recurrence. Together with the implementation of live-cell imaging,
495 SEM, OCT, and rheology, this model can provide important insights into the role of physical
496 characteristics of certain ECM components of OC microenvironments and their contribution to
497 OC outgrowth formation. The presented model of OC outgrowths is limited because it does not
498 recapitulate the full spectrum of ECM molecules associated with OC microenvironment.[58]
499 Future studies that quantitatively assess the ECM protein content *in vivo* would be necessary
500 to guide reconstruction of ECM microenvironment for further examination of ECM
501 contribution to OC growth.

502 **METHODS**

503 **Cell Culture**
504 Hey-A8 (obtained from Dr. Sumegha Mitra's laboratory, University of Indiana) and Tyk-nu
505 (obtained from Dr. Joan Brugge's laboratory, Harvard Medical School) cells were cultured in
506 a 1:1 ratio of Gibco™ Medium 199 (Gibco™) and MCDB105 (Sigma-Aldrich®) supplemented

507 with 5% heat-inactivated fetal bovine serum (HI-FBS; Gibco™), 1% (v/v) Penicillin-
508 Streptomycin (Gibco™) and 50 μg/ml plasmocin prophylactic (InvivoGen®). FNE cells
509 (obtained from Dr. Tan Ince's laboratory, Weill Cornell Medicine, New York) were cultured
510 in a 1:1 ratio of Medium 199 (HiMedia®) and DMEM/F12 (HiMedia®), 3% HI-FBS
511 (Corning®), 1% (v/v) Penicillin-Streptomycin (Sigma-Aldrich®), 0.5 ng/ml of 17 beta-estradiol
512 (US Biological®), 0.2 pg/ml of triiodothyronine (Sigma-Aldrich®), 0.025 μg/ml all-trans
513 retinoic acid (Beantown Chemical®), 20 μg/ml of insulin (Sigma-Aldrich®), 0.5 ng/ml of EGF
514 (Peprotech®), 0.5 μg/ml hydrocortisone (Sigma-Aldrich®), 25 ng/ml of Cholera Toxin
515 (Calbiochem) and 50μg/ml plasmocin prophylactic (InvivoGen®). ZT lung mesothelial cells
516 (obtained from Dr. Tan Ince's laboratory, Weill Cornell Medicine, New York) were from a
517 benign pleural effusion. These cells were immortalized by ectopic expression of the SV40 T
518 antigen and overexpression of human telomerase, which was fused to GFP.[59]Cell cultures
519 were tested for the presence of mycoplasma every 3 months using the Uphoff and Drexler
520 detection method.[60]

521 **IHC**
522 Formalin-fixed, paraffin-embedded (FFPE) patient-derived xenograft tissues (PDX) were a
523 kind gift from Dr. Ronny Drapkin, University of Pennsylvania. Sections were deparaffinized
524 in two xylene changes for 10 minutes each, then hydrated in a graded series of ethanol (100%
525 (v/v), 90% (v/v), 70% (v/v), 50% (v/v)) for 5 minutes each, and finally washed in ultrapure
526 water for 5 minutes. The ABC kit, Vectastain Elite (Vector Laboratories) was used, per the
527 manufacturer's recommendation. The primary antibodies used were anti-PAX8 (1:1000;
528 #10336-1-AP; Protein tech.), anti-LAMC1 (1:500; #HPA 001909; Sigma Aldrich). A
529 peroxidase substrate (ImmPACT DAB; #SK-4105; Vector Laboratories) was used to develop
530 and visualize staining under the microscope (Nikon ECLIPSE Ci-L equipped with a Nikon DS-
531 Fi3 camera). The slides were rinsed in water and dehydrated in a series of ethanol solutions of
532 increasing concentrations until 100% (v/v) ethanol was reached. The slides were then cleared
533 in xylene, mounted with a non-aqueous mounting medium (#H-5000; Vector Laboratories),
534 sealed using clear nail polish, and left to dry before imaging. Collagen staining was performed
535 using a Picrosirius red staining kit (#24901; Polysciences, Inc.) per the manufacturer's
536 recommendation. Deparaffinization and hydration were followed by 1-hour staining in
537 Picrosirius Red, washing in hydrochloric acid, dehydration, clearing in xylene, and mounting
538 as described above.

IHC Image Acquisition

Stained slides were scanned using an Olympus IX83 microscope equipped with a DP80 color camera and CellSens software. Based on scanned slides, ROIs were identified and recaptured using a Nikon Eclipse equipped with a DS-Fi3 color camera and NIS Elements D software. Images were saved in tag-image file format TIFF for further processing.

IHC Image Processing

As previously described,[61] RGB images were converted, using a weighted RGB conversion option in FIJI (Fiji is just ImageJ) software,[62] to an 8-bit grayscale range representing values between black (0) and white (255). To clean out the white noise from the background, images were inverted and multiple ROIs representing tumor, stroma, or areas without tissue were selected. Mean gray values (between 0-255) were calculated for each ROI and subsequently plotted after subtracting the background signal of area without tissue. Statistical analysis was performed using the Ordinary One-way ANOVA function of GraphPad Prism [version 9.1.0 for Windows, GraphPad Software, San Diego, California USA, www.graphpad.com].

Pathology Scoring of Laminin γ1 Expression in Human Tumors

Intensity profiles of IHC were qualitatively scored as strong (+3), moderate (+2), weak (+1), and negative (0). IHC results were recorded by a pathologist using H-scores, which were calculated by the following formula: H-score = [(0 x % negative cells) + (1 x %weakly positive cells) + (2 x %moderately positive cells) + (3 x %strongly positive cells). Data are represented as dot plots of H-scores for matched biopsy. Since the data falls into a category of a non-normal distribution, a (nonparametric) Wilcoxon rank-sum test was used to calculate significant differences between pre- and post-therapy specimens.

ECM Reconstitution

One hundred cells per well were seeded on ultra-low attachment 96-well plates (Corning®), immediately centrifuged at 900 RPM for 3 minutes, and allowed to incubate until the following day. On the following day, on ice and using prechilled pipette tips, 100 μL of 4% (v/v), or 50% (v/v) Matrigel® (MG) (Corning®) was added to each well containing 100 μL of clustered spheroid, with a final culture volume of approximately 200 μL and final MG concentration of approximately 2% (v/v) or 25% (v/v). Matrigel lot numbers; 9294001; 9028255; 1244002; 1362001; 0288002 were used. These lot numbers represent catalogue number 354230.

Live-Cell Imaging of 3D Cultures

Ultra-low adhesion 96-well plates containing ECM reconstituted cell cultures were placed within an Agilent® BioTek® LionHeart™ FX long-term imaging chamber equipped with enclosed optics, temperature, and gas exchange controls. Individual spheroids were imaged for up to 7 days with images being captured at indicated time intervals. Multiple XYZ planes of spheroids were acquired simultaneously.

Quantification of Outgrowth Protrusion Frequency

To quantify the frequency of outgrowth protrusions by spheroids representing various FNE and OC cell lines, different laboratory members set up at least thirty spheroid cultures reconstituted with 2% (v/v) MG were prepared for each experiment. Outgrowths were subjectively defined as distinct cell populations that appeared outside of the main spheroid. Scoring was performed using a Nikon 2000 tissue culture microscope with a 10X objective.

Mesothelial Clearance Assay

Mesothelial cells were plated on glass-bottom dishes (Mat-TEK Corporation), which had been coated with 5 μg/mL of fibronectin (Sigma-Aldrich®). GFP-expressing ZT cells were maintained in culture to form a confluent monolayer (up to 24 hours after plating). Spheroids generated with Hey-A8 were cultured for a period of seven days. Using a dissecting microscope and surgical scalpel, outgrowths were mechanically detached from their main spheroid and subsequently transferred to the co-culture containing the mesothelial monolayers. In the co-culture experiments, spheroids and their respective outgrowths were allowed to interact with a confluent mesothelial monolayer expressing green fluorescent protein (GFP). Co-culture was imaged at 1-hour intervals for up to 72 hours using an Agilent® Biotek® LionHeart™ FX (BioTek) inverted Motorized Widefield Fluorescence Microscope. Mesothelial clearance was quantified as previously described.[39] The non-fluorescent area in the GFP images of the last time point of the assay, created by the penetrating cell cluster into the GFP mesothelial monolayer, was measured using FIJI [62] software. The non-fluorescent area of the final timepoint was then normalized to the area of the spheroid at the initial timepoint from the bright field channel acquisition. Data distribution and statistical analysis were conducted using GraphPad Prism [version 9.1.0 for Windows, GraphPad Software, San Diego, California USA, www.graphpad.com].

Cell Viability and PI Incorporation Assay

The viability of both spheroid and outgrowth were quantified with a propidium iodide (PI) incorporation assay. PI is a red fluorescent dye that intercalates into double-stranded DNA but is only permeable through the compromised plasma membranes of dying/dead cells. Hey-A8 spheroids were cultured in 2% (v/v) MG and allowed to incubate for a period of 7 days. Hey-A8 spheroids were stained with PI to a final concentration of 2 µg/mL, then allowed to incubate for 30 minutes in dark. Hey-A8 spheroids were subsequently imaged with an Agilent® BioTek® LionHeart™ FX automated microscope. Z-projected images were captured with a 4X objective in both bright field and PI (590 γ excitation spectra – Texas red) channels. Following image acquisition, Z-projections for each spheroid were opened in FIJI[62] and subjected to the following: Z-projections were stacked, regions of interest (ROIs) for each bright field acquisition were manually selected for both the spheroid and its associated outgrowth and selected ROIs were then superimposed over the paired PI acquisition of the same spheroid. From each Texas red channel acquisition, the mean intensity of PI was measured for both ROIs (spheroid and outgrowth) and normalized to the area of the respective ROI, thereby yielding PI mean intensity for the area of the spheroid, and for the area of the outgrowth. PI mean intensity were plotted, and statistical analysis was conducted using GraphPad Prism [version 9.1.0 for Windows, GraphPad Software, San Diego, California USA, www.graphpad.com].

Determination of Outgrowth Length and Cellular Structure Area

GEN5 image analysis software (BioTek) was used to quantify outgrowth length and ImageJ was employed to analyze spheroid size. Before quantification, a series of bright field images, representing multiple XYZ planes of a discrete cellular structure, was collapsed to generate maximal projections of a spheroid and its protruding outgrowth. Outgrowth protrusion was identified as a structure that extended beyond the main spheroid body, and a line was drawn from the tip across the longer axis of the outgrowth, terminating at the junction between outgrowth protrusion and the spheroid. The size of the cellular structure was calculated using an in-house ImageJ macro. Binary masks were created to separate a single cellular structure from the non-cellular background.

Cryo-SEM Sample Preparation and Imaging

All samples for cryo-scanning electron microscopy (SEM) were prepared by using a Leica EM HPM100 high-pressure freezing (HPF) system. The HPF planchettes were washed in ethanol

634 and exposed to an oxygen plasma for ten minutes before use. The frozen-hydrated samples

635 were stored in liquid nitrogen. A Leica VCT-100 system was used for subsequent cryo-transfer

636 and cryo-imaging. Samples were transferred and coated with sputtered gold (Au) (2.5 nm)

637 under cryogenic conditions (T < -135 °C) by a Leica EM MED020 system. Before SEM

638 imaging, sublimation was used to create topographic contrast by slightly warming frozen-

639 hydrated samples. SEM imaging was done by using a Zeiss Auriga Crossbeam FIB-SEM

640 equipped with a Schottky field-emission electron gun (FEG) and an Oxford Max-80 ultrathin

641 window (UTW) silicon-drift detector (SDD) interfaced to an Oxford INCA EDS system.

642 Secondary electron imaging (Everhart-Thornley detector) was done by using 2 keV electrons

643 and a 2.5 nm Au coating.

Assessment of ECM network in MG with OCT

645 A spectral-domain OCT system with a central wavelength of approximately 850 mm was used

646 for MG imaging. The system provides an axial resolution of approximately 9 μm in biological

647 samples (1.4 refractive indexes assumed) and a transverse resolution of approximately 5 μm.

648 Parameters for imaging of 2% (v/v) and 25% (v/v) MG samples were kept identical. Data

649 processing focused on the characterization of the spatial frequency over depth, similar to a

650 previously developed method.[63] Briefly, with the dB intensity A-scan and the identified

651 sample surface, the intensity profile over 0.4 mm starting at approximately 26 μm below the

652 sample surface was utilized for analysis. The slope of the signal that represents the optical

653 attenuation over depth was removed. Through a fast Fourier transform, the amplitude spectrum

654 of the spatial frequency was obtained, and an exponential fit of the local peaks was performed.

655 The exponential decay coefficient was calculated as the measure of the spatial frequency over

656 depth and was used to compare the 2% (v/v) and 25% (v/v) MG samples. A higher decay

657 coefficient represents relatively stronger low-frequency components of the spatial frequency

658 spectrum.

Rotational Rheology

660 The linear viscoelastic material functions, the storage modulus, G', and the loss modulus, G",

661 of the 2% (v/v), 25% (v/v) MG samples, as well as ascitic fluids isolated from OC patients,

662 were characterized using an Advanced Rheometric Expansion System (ARES) rheometer

663 available from TA Instruments of New Castle, DE. The rotational rheometer was used with

664 stainless steel parallel disks with a 25 mm diameter and had a force rebalance transducer 0.2K-

665 FRTN1. The actuator of the ARES is a DC servomotor with a shaft supported by an air bearing

666   with an angular displacement range of 5×10^{-6} to 0.5 rad, and an angular frequency range of

667   1×10^{-5} to 100 rad/s. The angular velocity range is 1×10^{-6} to 200 rad/s. The sample loading

668   procedure was the same for all the experiments, and the gap height between two disks was kept

669   constant at 1 mm. A sufficient volume of sample was used to fill the gap between parallel disks,

670   and the linear viscoelastic properties of the samples were collected as a function of frequency

671   at a constant strain of 50% and room temperature. The samples were not pre-sheared. For

672   discussion of dynamic property characterization of complex fluids see, for example, Bird, R.B.,

673   Armstrong, R.C., and Hassager, O. "Dynamics of Polymeric Liquids. Wiley, 1987."

674   **Matrigel® (MG) Overlay**

675   MG was diluted with an appropriate prechilled medium and a sterile and precooled pipette tip

676   to a final concentration of 2% (v/v) or 25% (v/v). After cell attachment, the medium was

677   aspirated from the 96-well plates and the medium/MG mixture was overlaid onto the cell

678   monolayer. MG-treated cultures were allowed to incubate overnight before proceeding with

679   live-cell time-lapse imagining or incubated for 72 h before fixation and IF staining. The

680   procedure as described produces a coat of matrix that gels at 37°C and attaches to the upper

681   surface of the monolayer.[41]

682   **Processing of spheroids for EdU labeling**

683   Hey-A8 spheroids were fixed in a 4% (v/v) paraformaldehyde solution (Sigma-Aldrich®) and

684   dehydrated in ethanol. HistoGel™ (Thermo Fisher Scientific®) was liquified, and spheroids

685   were mixed with HistoGel™ and left to solidify in a biopsy cassette. HistoGel™ blocks were

686   fixed in 10% (v/v) neutral-buffered formalin overnight, then dehydrated in ethanol and cleared

687   in xylene. Processed HistoGel™ blocks were then embedded in paraffin and stored at -20 °C

688   until the time of sectioning. Paraffin blocks were sectioned at a thickness of 5 μm using a

689   microtome (Leica).

690   **EdU incorporation assay**

691   MG reconstituted Hey-A8 cells were incubated with 10 mM Click-iT™ EdU [Thermo Fisher

692   Scientific®, catalog #: C10340] for 4 hours. Cells were fixed with 4% (v/v) PFA for 1 hour at

693   room temperature, embedded into HistoGel™, and sectioned. Sections were permeabilized

694   with 1X PBS containing 0.5% (v/v) Triton-X. Residual Triton-X was removed by washing

695   twice with 1X PBS supplemented with 3% (w/v) BSA. To label the incorporated EdU, sections

696   were incubated in the dark for 30 minutes with a Click-iT reaction cocktail prepared fresh (<15

697   minutes before labeling). The Click-iT reaction cocktail was then removed, and sections were

698   washed with 1X PBS. To label total cell nuclei, sections were incubated in the dark with 10

699   μg/mL Hoechst 33342 in 1X PBS for 30 minutes. After washing out the Hoechst dye with 1X

700   PBS, sections were mounted with aqueous mounting media and sealed by coverslips. The

701   sections were imaged on ZEISS LSM-880 confocal microscope using a 10X objective. Images

702   of EdU-labeled nuclei were acquired using far-red laser illumination ($\lambda = 647$ nm) and total

703   nuclei were captured by violet-blue laser illumination ($\lambda = 405$ nm). Images were analyzed

704   using the open-source software FIJI.[62]

705   **Cell proliferation, cell motion imaging, and quantifications**

706   Monolayers of FNE-m-p53 or Hey-A8 cells expressing GFP or mKO2, respectively, were

707   overlaid with MG. Time-lapse imaging was performed on an Agilent® BioTek® Lionheart™

708   FX automated microscope using a 10X objective and a maximal capture interval of 22 minutes.

709   After the acquisition, time-lapse images were background subtracted (radius 50 pixels) using

710   FIJI[62] image analysis software. To analyze cell proliferation and movement within MG-

711   overlaid cell cultures, we used an ImageJ plugin, TrackMate,[64] to perform single-particle

712   tracking (SPT). TrackMate offers multiple modes of analysis and based on both our cell size

713   and the relatively slow movement of cells, we selected and applied the following parameters

714   in TrackMate: LoG (Laplacian of Gaussian) detector, the spot diameter of 35 pixels, threshold

715   of 10, median filter and LAP tracker with 15-pixel frame linking, 2-frame gap distance and

716   track-segment splitting. We extracted the spot count in the desired time frames (one count every

717   12 hours or 33 frames) to obtain the number of cells or spots in the region of interest at those

718   time points. We then divided the number of cells in each time point by the number of cells at

719   the starting time point (time = 0) to normalize and plot it as a measure of fold change. An

720   unpaired, two-tailed t-test was used to assess the significance of fold change in cell number

721   between the first and final time points. Plotting and statistical analysis were conducted using

722   GraphPad Prism [version 9.1.0 for Windows, GraphPad Software, San Diego, California USA,

723   www.graphpad.com]. To quantify track displacement, we calibrated the images by converting

724   output in pixels into micrometers, and frames into hours. For visualization of local tracks, we

725   used 50-frame-depth-, time-color-coded tracks overlayed on a GFP or RFP channel time-lapse.

726   For trajectory classification, we used the TraJClassifier plugin.[65] The plugin uses TrackMate

727   output data and trajectories and computes a confinement ratio representing cell directionality

728   over time. After all the trajectories were computed into confinement ratios, we plotted the data

729   using Prism GraphPad Prism 9.1.0. Trajectories from multiple fields of view were plotted and

730   directed-motion trajectories were represented as confinement ratio values. Each dot in a dot

731 plot represents one field of view with the horizontal line depicting the mean of all fields of
732 view per condition. Statistical analysis was computed using an unpaired, two-tailed t-test.

733 **Ascites and solid carcinoma tissue collection**
734 Ascitic fluids were collected from patients with ovarian cancer either by paracentesis under
735 local anesthesia or at the very beginning of surgery. Ascites was centrifuged at 1,100 x g for
736 10 min at room temperature to remove cell clusters, then aliquoted and stored at -80 °C until
737 analysis. All solid tissue collections were performed during surgery. All procedures performed
738 in studies involving human participants were following the ethical standards of the institutional
739 and national research committee and with the 1964 Helsinki declaration and its later
740 amendments or comparable ethical standards. Patients provided a signed informed consent,
741 approved by the Ethics Review Board of Poznań University of Medical Sciences (Consent No
742 737/17).

743 **Immunofluorescence staining**
744 MG overlayed 2D cultures or spheroid cultures were washed thrice with PBS, fixed in 4%
745 paraformaldehyde for 15-30 min at room temperature. Following blocking with 2.5% normal
746 goat serum for 60 min, cells were incubated with indicated primary antibodies for 1 h at room
747 temperature. Following PBS washes, cells were incubated with secondary antibody tagged with
748 fluorescein diluted at 1:500 in PBS. For nuclear staining, Hoechst was used. Immunostained
749 samples were examined under ZEISS LSM-880, the confocal laser scanning microscope
750 (CLSM).

751 **N-cadherin quantification**
752 Still images of HeyA8 spheroids reconstituted with 2% or 25% MG and stained with N-
753 cadherin and DAPI were acquired on laser scanning confocal microscope (ZEISS LSM 880)
754 using 20x objective. Still images were collected as Z-stacks which were later projected after
755 acquisition using standard deviation projection mode with image analysis software Fiji.[62] As
756 the Hey-A8 spheroids were too large to fit into a single image frame using the 20x objective,
757 we focused on imaging the spheroid edges, capturing different edges of spheroids in multiple
758 frames. To quantify the level of N-cadherin staining strictly at the spheroid edge, we manually
759 selected the region of the edge and measured the raw integrated density of the N-cadherin
760 channel (547 nm) and the DAPI channel (405 nm). To account for the different size of the
761 region and varying number of cells in each region, we first normalized the raw integrated
762 density to the region area (in pixels) and then normalized that value from the N-cadherin

763   channel (547 nm) to the DAPI channel (405 nm). Normalized N-cadherin value was plotted

764   using Prism GraphPad Prism [version 9.1.0 for Windows, GraphPad Software, San Diego,

765   California USA, www.graphpad.com]. Each value on the plot represents one spheroid edge

766   with the bar height depicting the mean of all edges taken per condition with error bars as

767   standard deviation. A total of 31 – 43 edges were quantified per condition, corresponding to 16

768   – 19 Hey-A8 spheroids per condition. Statistical analysis was performed using the Ordinary

769   One-way ANOVA function of GraphPad Prism [version 9.1.0 for Windows, GraphPad

770   Software, San Diego, California USA, www.graphpad.com].

771   **Focal adhesion quantification**

772   Still images of FNE m-p53 and Hey-A8 cells overlayed with 2% or 25% Matrigel and stained

773   with paxillin, phalloidin (F-actin) and Hoechst 33342 were acquired on laser scanning confocal

774   microscope (ZEISS LSM 880) using 20x objective. Still images were collected as Z-stacks

775   which were later projected after acquisition using maximum projection mode with image

776   analysis software Fiji.[62] To quantify number of focal adhesion foci we used an ImageJ plugin

777   TrackMate,[64] a readily available tool to perform a range of operations from particle detection

778   to single particle tracking (SPT). TrackMate offers multiple modes of analysis and based on

779   intensity and size of our paxillin foci, we selected and applied the following parameters in

780   TrackMate: LoG (Laplacian of Gaussian) detector, estimated object diameter of 1 micron,

781   quality threshold 20, with applied median filter. We applied this setting to each ROI we imaged.

782   To account for the varying number of cells in each ROI, we normalized the total number of

783   focal adhesion (paxillin) foci detected to the total number of nuclei in the respective ROI, which

784   we counted using the TrackMate thresholding detector with auto intensity threshold.

785   Normalized number of focal adhesion foci was then plotted using Prism GraphPad Prism

786   [version 9.1.0 for Windows, GraphPad Software, San Diego, California USA,

787   www.graphpad.com]. Each value on the plot represents one ROI with the bar height depicting

788   the mean of all ROIs per condition, with error bars as standard deviation. A total of 10 ROIs

789   were quantified per condition, ranging between 12 – 376 cells per ROI. Statistical analysis was

790   performed using the Ordinary One-way ANOVA function of GraphPad Prism [version 9.1.0

791   for Windows, GraphPad Software, San Diego, California USA, www.graphpad.com].

792   **PAX8 quantification for stroma invasion**

793   Using FIJI (Fiji is just ImageJ) software,[62] multiple ROIs representing tumor, stroma, or Villi

794   small intestine were selected. Integrated density "IntDen" (the product of Area and Mean Gray

795 Value)[62] was calculated for each ROI subsequently plotted. Statistical analysis was performed

796 using the Ordinary One-way ANOVA function of GraphPad Prism [version 9.1.0 for Windows,

797 GraphPad Software, San Diego, California USA, www.graphpad.com]. ANOVA was followed

798 by Tukey post-hoc analysis.

799 **Statistical analysis**

Figure	Pre-processing	Data presentation	Sample size (n) / ROI = region of interest (microscopic field of view)	Statistical methods	Software used
1-G	Intensity values normalized to background level (area without tissue)	All data are shown with bars indicating mean ± SD	Each data point is one ROI. 51 ROI/ condition (tumor and stroma)	An unpaired, two-tailed, non-parametric, Mann-Whitney test	Prism (GraphPad)
1-H	Intensity values normalized to background level (area without tissue)	All data are shown with bars indicating mean ± SD	Each data point is one ROI. 59 ROI/ condition (tumor and stroma)	An unpaired, two-tailed, non-parametric, Mann-Whitney test	Prism (GraphPad)
1-I	Intensity values normalized to background level (area without tissue)	All data are shown with bars indicating mean ± SD	Each data point is one ROI. 38 ROI/ condition (tumor and stroma)	An unpaired, two-tailed, non-parametric, Mann-Whitney test	Prism (GraphPad)

1-J	Intensity values normalized to background level (area without tissue)	All data are shown with bars indicating mean ± SD	Each data point is one ROI. 45 ROI/ condition (tumor and stroma)	An unpaired, two-tailed, non-parametric, Mann-Whitney test	Prism (GraphPad)
2-D	None H-score = [(0 x % negative cells) + (1 x %weakly positive cells) + (2 x %moderately positive cells) + (3 x %strongly positive cells).	All data are shown with bars indicating mean ± SD	Each data point is a patient sample represented by the H-score. N=3 patient samples	Wilcoxon sum rank	MATLAB
2-E	Intensity values normalized to background level (area without tissue)	All data are shown with bars indicating mean ± SD	Each data point is one ROI BEFORE=82 AFTER=160	An unpaired, two-tailed, parametric student t-test with Welch's correction	Prism (GraphPad)
3-C	Final spheroid area was normalized to initial spheroid area within the timelapse movie	All data are shown with bars indicating mean ± SD	Each data point is one spheroid. 8 FNE spheroids vs. 10 FNE m-p53 spheroids	An unpaired, two-tailed, parametric student t-test with Welch's correction	Prism (GraphPad)
3-D	None	All data are shown with bars indicating mean	>30 spheroids	None	Prism (GraphPad)

3-E	None	All data are shown with bars indicating mean	20-30 spheroids	None	Prism (GraphPad)
4-C	Cleared (non-GFP) area of mesothelial cell monolayer at last time point of the experiment were normalized to the primary spheroid area	All data are shown with bars indicating mean ± SD	Each data point is one structure. 69 spheroids vs. 43 outgrowths	An unpaired, two-tailed, non-parametric, Mann-Whitney test	Prism (GraphPad)
4-E	RFP intensity values (of main spheroid or outgrowth) were normalized to the area of the spheroid or outgrowth	All data are shown with bars indicating mean ± SD	Each data point is one structure. 21 spheroids vs. 22 outgrowths	An unpaired, two-tailed, non-parametric, Mann-Whitney test	Prism (GraphPad)
5-A	None	All data are shown with bars indicating mean ± SD	Each data point is one structure. 11 spheroids in 2% MG vs. 8 spheroids in 25% MG	An unpaired, two-tailed, parametric student t-test with Welch's correction	Prism (GraphPad)
5-B	None	All data are shown with bars indicating mean ± SD	Each data point is one spheroid structure. 19 spheroids in 2% MG vs.	An unpaired, two-tailed, parametric student t-test with Welch's correction	Prism (GraphPad)

			20 spheroids in 25% MG		
6-A-F	None	All data points are shown as the mean and SD of triplicate measurement	total triplicate measurement 91- 2% MG 41- 25% MG 91- Ascites	None	Prism (GraphPad)
7-C, E	None	All data points are shown with bars indicating mean ± SD	Each dot represents one ROI that contains 20-100 cells. Two independent experiments were performed with a total of 12-30 ROI/ condition (2% vs. 25% MG)	An unpaired, two-tailed, parametric student t-test with Welch's correction	Prism (GraphPad)
S1-A	None	All data are shown with bars indicating mean ± SD	Each data point is one spheroid. 10 spheroids in 2% MG vs. 8 spheroids in 25% MG	An unpaired, two-tailed, parametric student t-test with Welch's correction	Prism (GraphPad)
S1-B	None	All data are shown with bars indicating	Each data point is one spheroid. 10 spheroids	An unpaired, two-tailed, parametric student t-test	Prism (GraphPad)

		mean ± SD	in 2% MG vs. 16 spheroids in 25% MG	with Welch's correction	
S2	Normalization of N-cadherin signal to Hoechst signal in same ROI	All data are shown with bars indicating mean ± SD	Each data point is one structure. 19 spheroids / condition (2% vs. 25% MG)	An unpaired, two-tailed, non-parametric, Mann-Whitney test	Prism (GraphPad)
S3-B	Normalization of cell number in end frame to cell number in the first frame in the same ROI (fold change)	All data are shown with bars indicating mean ± SD	Each dot corresponds to one ROI containing 2-116 cells. Two independent experiments were performed with a total of 15-20 ROI / condition (2% vs. 25% MG)	An unpaired, two-tailed, parametric student t-test with Welch's correction	Prism (GraphPad)
S3-C	Normalization of cell number in end frame to cell number in the first frame in the same ROI (fold change)	All data are shown with bars indicating mean ± SD	Each dot corresponds to one ROI containing 3-108 cells. Two independent experiments were performed with a total of 15 ROI /	An unpaired, two-tailed, parametric student t-test with Welch's correction	Prism (GraphPad)

			condition (2% vs. 25% MG)		
S3-E	Normalization of the number of EdU positive nuclei to the total number of nuclei	All data are shown with bars indicating mean ± SD	23 HeyA8 spheroids in 2% MG vs. 34 HeyA8 spheroids in 25% MG	An unpaired, two-tailed, non-parametric, Mann-Whitney test	Prism (GraphPad)
S4	None	All data points are shown as the mean and SD of triplicate measurement	total triplicate measurement 61- Ascites 2&3	None	Prism (GraphPad)
S6	Normalization of the number of paxillin foci in ROI to the number of nuclei in the same ROI	All data are shown with bars indicating mean ± SD	Each data point is one ROI containing 31-376 cells. Two independent experiments were performed with a total of 10 ROI / condition (2% vs. 25% MG)	An unpaired, two-tailed, parametric student t-test with Welch's correction	Prism (GraphPad)
S7	Normalization of the number of paxillin foci in ROI to the	All data are shown with	Each data point is one ROI (12-149	An unpaired, two-tailed, parametric	Prism (GraphPad)

	number of nuclei in the same ROI	bars indicating mean ± SD	cells). Two independent experiments were performed with a total of 9 ROI/ condition (2% vs. 25% MG)	student t-test with Welch's correction	
S8	Logarithmic transformation (log base 10) of integrated density values	All data points are shown as median and quartiles	Each data point is one ROI. Tumor 66 ROI Stroma 20 ROI Villi 20 ROI	Ordinary one-way ANOVA test was used to examine statistical differences between data sets. ANOVA was followed by Tukey post hoc analysis; Tumor vs. Stroma P < 0.001, Tumor vs. Villi small intestine P < 0.001, Stroma vs. Villi small intestine P > 0.999.	Prism (GraphPad)

800

801 **Reagents and materials:**

Item	Cat. No.	Vendor
PAX8	10336-1-AP	Protein tech.
LAMC1	HPA 001909	Sigma Aldrich

VECTASTAIN Elite ABC HRP	PK-6101	vector laboratories
ImmPACT DAB	SK-4105	vector laboratories
Hematoxylin QS	H-3404-100	vector laboratories
picrosirius red	24901	Polysciences Inc.
non-aqueous mounting medium	H-5000	vector laboratories
Aqueous mounting medium	H-5501	vector laboratories
Medium 199	AT014-5L	Himedia
MCDB105	M6396-10X1L	Sigma Aldrich
Heat Inactivated Fetal bovine serum	10438-026500mL	Gibco
Plasmocin prophylactic	ant-mpp	In vivo Gen
Penicillin-Streptomycin	30-002-CI	Corning
DMEM/F12	AT147A-10L	Himedia
17 beta-estradiol	15600	USB
triiodothyronine	T6397-100MG	Sigma Aldrich
all-trans retinoic acid	216220-250MG	BeanTown Chemical
EGF	100-26-25UG	Peprotech
hydrocortisone	H088-1G	Sigma Aldrich
cholera toxin	C8052	Sigma Aldrich
Matrigel	354230	Corning
ultra-low attachment 96-well plates	7007	Corning
Trypsin	25-053-Cl	Corning
Insulin	I9278-5ML	Sigma Aldrich
Histogel	HG-4000-012	Thermo Scientific
Formalin	VT450C	Lam Chem
Xylene	89370-088	VWR
Ethanol	241000200CSGL	GREENFIELD GLOBAL INC
PBS	21-040-CV	Corning
Propidium iodide	P1304MP	Molecular Probes
EDU kit	C10640	LIFE TECHNOLOGIES
N-Cadherin	C3865	Sigma Aldrich
Paxillin	610051	BD Pharmingen
Phalloidin	A12380	ThermoFisher
Alpha smooth muscle actin	ab7817	Abcam

Triton-X and Tween-20	0777-1L	VWR
Alexa fluor 488	A11029	Invitrogen
Alexa fluor 546	A11003	Invitrogen
Alexa fluor 568	A-11031	Invitrogen

Author Contributions: S.A., T.P. and M.I. designed and conceptualized the studies with significant input from S.F., P.B., D.C., and D.K. IHC analysis of human tumors and PDX tissue sections were performed by S.A., and T.P. performed cell tracking experiments and image quantification. S.F. performed mesothelial clearance assays. P.B., L.Q., and D.Kh. designed and performed shear-stress rheometric analyses. P.B. and W.L. designed and performed electron microscopy experiments. M.R., P.J., E.D., E.N-M. and M.P-Z., identified human tumor samples and performed pathologic analysis of laminin γ1 expression in tumors representing disease before and after chemotherapy. S.A., T.P., and M.I. wrote a manuscript with significant input (methodology description) from S.F., P.B., L.Q., D.Kh., S.W., and M.P-Z.

Competing Interest Statement. The authors declare no competing interests.

820 **Supplementary Figures**
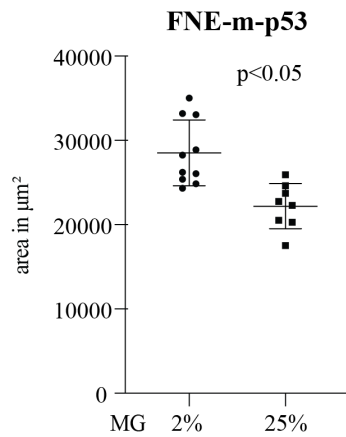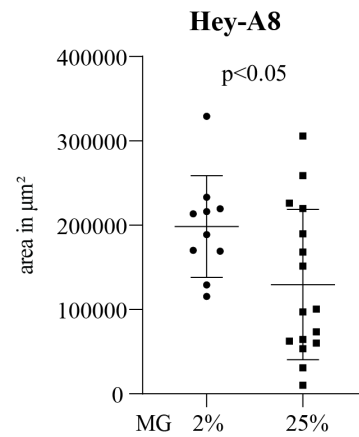
821 **S. Figure 1.** Elevation of ECM concentration suppresses FNE-m-p53 and Hey-A8 structure expansion.
822 Quantification of an area in (**A**) FNE-m-p53 or (**B**) Hey-A8 spheroids reconstituted with 2% or 25% MG. Each
823 dot represents a spheroid (8-16 spheroid/condition) measured 9 days after starting the culture. All data are shown
824 with bars indicating mean ± SD. An unpaired, two-tailed, parametric student t-test with Welch's correction was
825 used to examine statistical differences between data sets.
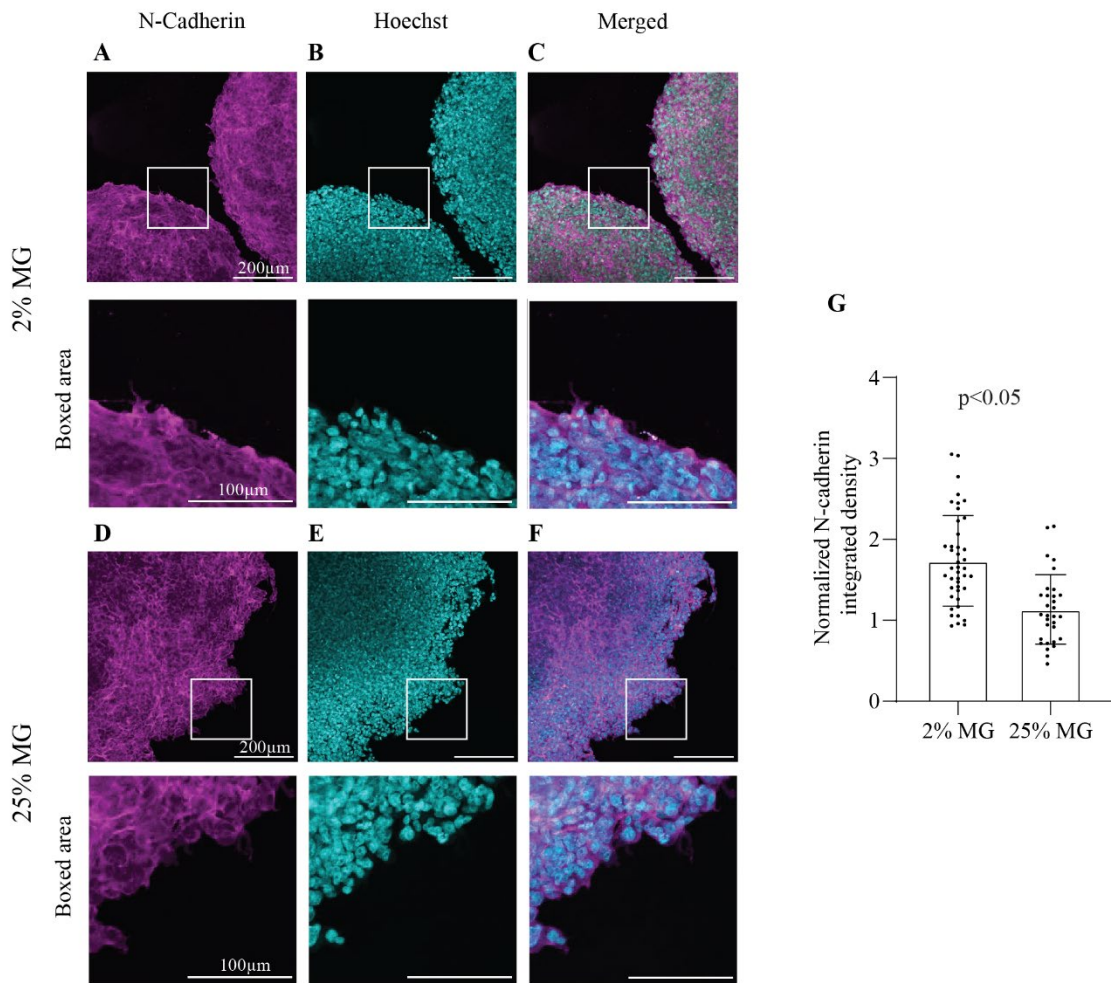
S. Figure 2. Increased ECM concentration leads to reduced N-cadherin expression at the 3D OC spheroid surface edge. Hey-A8 spheroids were reconstituted with (**A, B, C**) 2% MG or (**D, E, F**) 25% MG and stained with (**A, D**) antibodies against N-cadherin, and (**B, E**) Hoechst 33342 dye. (**G**) Quantification of N-cadherin expression on the edges of Hey-A8 spheroids reconstituted with 2% or 25% MG, respectively. Each data point is one ROI (1-5 spheroid edges). Nineteen spheroids were analyzed/ condition. All data points are shown with bars indicating mean ± SD. An unpaired, two-tailed, non-parametric, Mann-Whitney test was used to examine statistical differences between data sets. Integrated density values of N-cadherin were normalized to integrated density values of corresponding Hoechst 33342 signals.
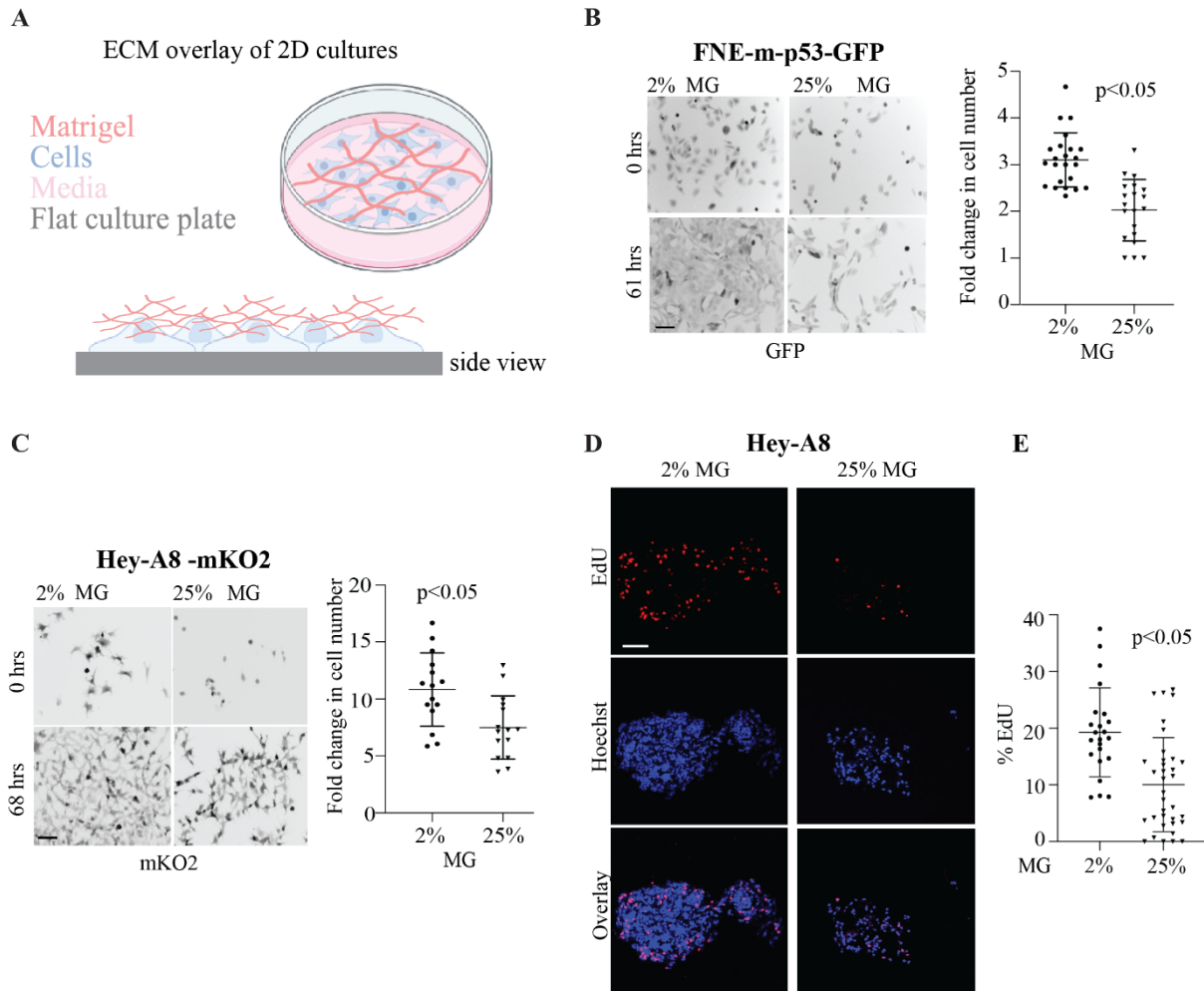
834

835 **S. Figure 3.** Elevation of ECM concentration suppresses FNE-m-p53 and Hey-A8 cell proliferation. (**A**) Cartoon

836 representation of the experimental design for ECM overlay of cell monolayers. Created with BioRender.com.

837 Representative fluorescent images of (**B**) FNE-m-p53 expressing GFP or (**C**) Hey-A8 cells expressing mKO2

838 monolayers overlayed with 2% or 25% MG. Dot plots represent a fold-change increase in cell number over time.

839 Each dot corresponds to one field of view (FOV) containing (2-116 cells) and (3-108 cells) in B and C, with a

840 total of 15-20 FOVs/ condition (2% & 25%). Data points are presented as mean ± SD. An unpaired, two-tailed,

841 parametric student t-test with Welch's correction was used to compute the statistical difference. (**D**)

842 Representative fluorescent images of EdU and Hoechst in Hey-A8 spheroids reconstituted with 2% and 25% MG.

843 Spheroids were processed 9 days after starting the culture. (**E**) The dot plot represents the fraction of EdU-positive

844 cells. Each dot represents a spheroid; total spheroids 23 and 34 in 2% and 25%, respectively. All data points are

845 shown with bars indicating mean ± SD. An unpaired, two-tailed, non-parametric, Mann-Whitney test was used to

846 compute the statistical difference. Scale bars are 100 μm.
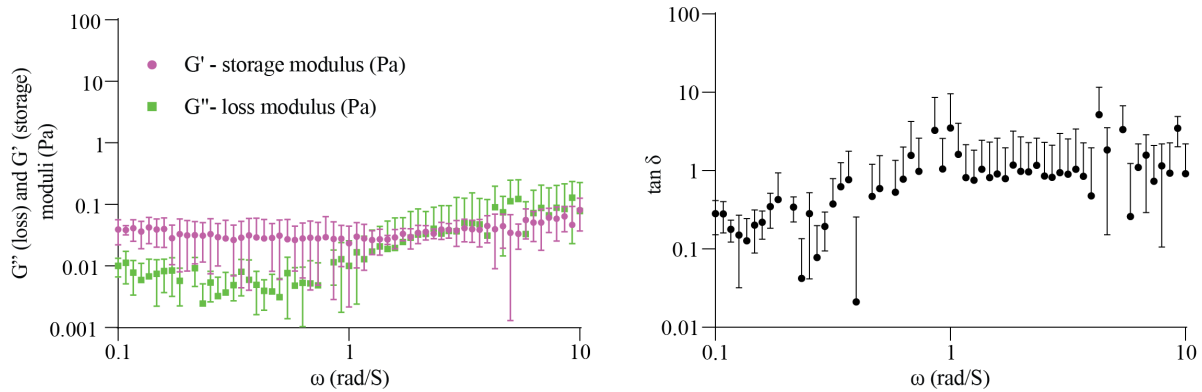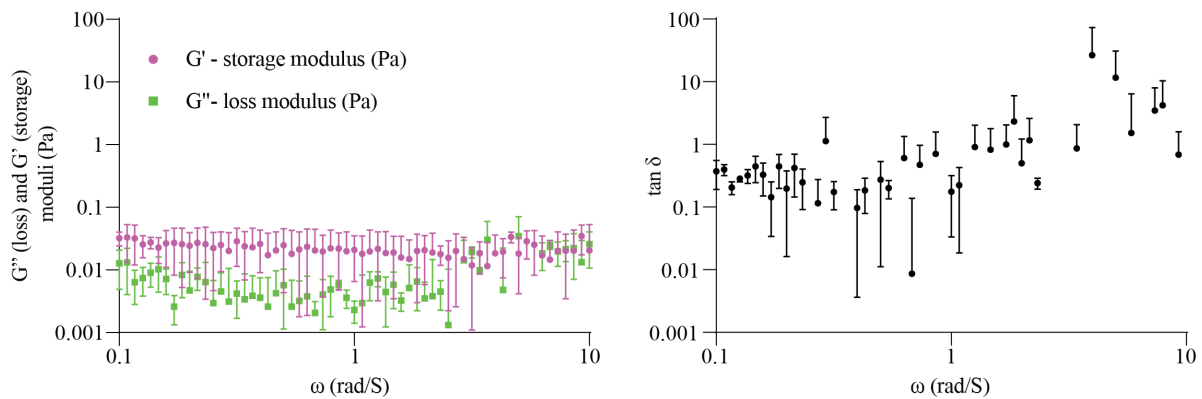
S. Figure 4: Viscoelastic properties of ascitic fluid samples isolated from OC patients with relapsed disease. Graphs represent the measurements of storage moduli (elastic), loss moduli (viscous), and tan δ (loss moduli divided by storage moduli) of (**A&B**) patient-derived ascites samples. Each data point represents the mean and SD from triplicate measurements with a total of 61 measurements.
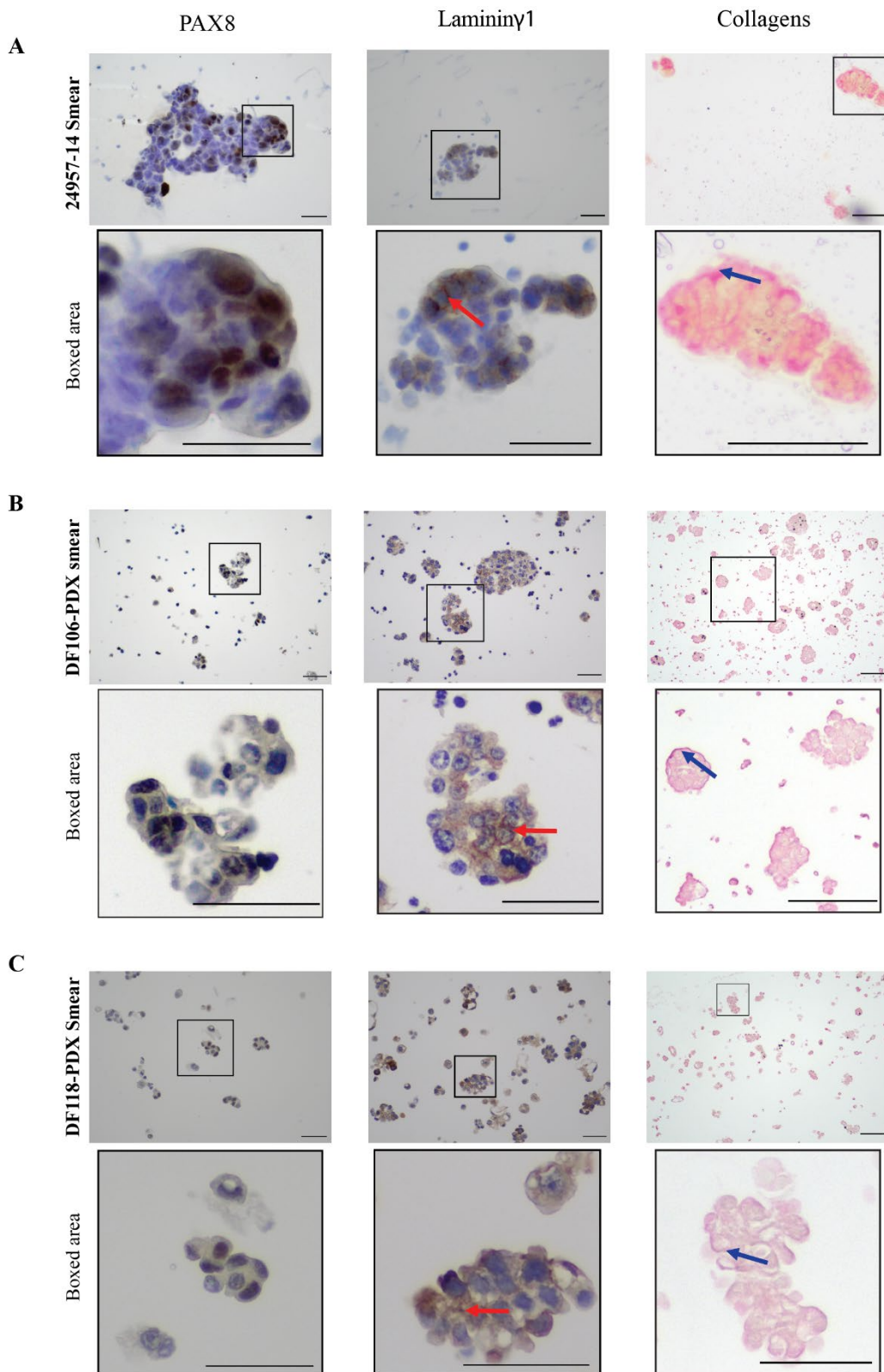
851 **S. Figure 5.** Laminin γ1 and collagen expression in OC clusters isolated from human or mouse ascites.

852 Immunocytochemistry of Laminin γ1 and collagen in PAX8-positive (**A**) human, (**B & C**) PDX ascitic smears.

853 Red arrows point to lamininγ1. Blue arrows point to collagen. Scale bars are 50 μm.

854
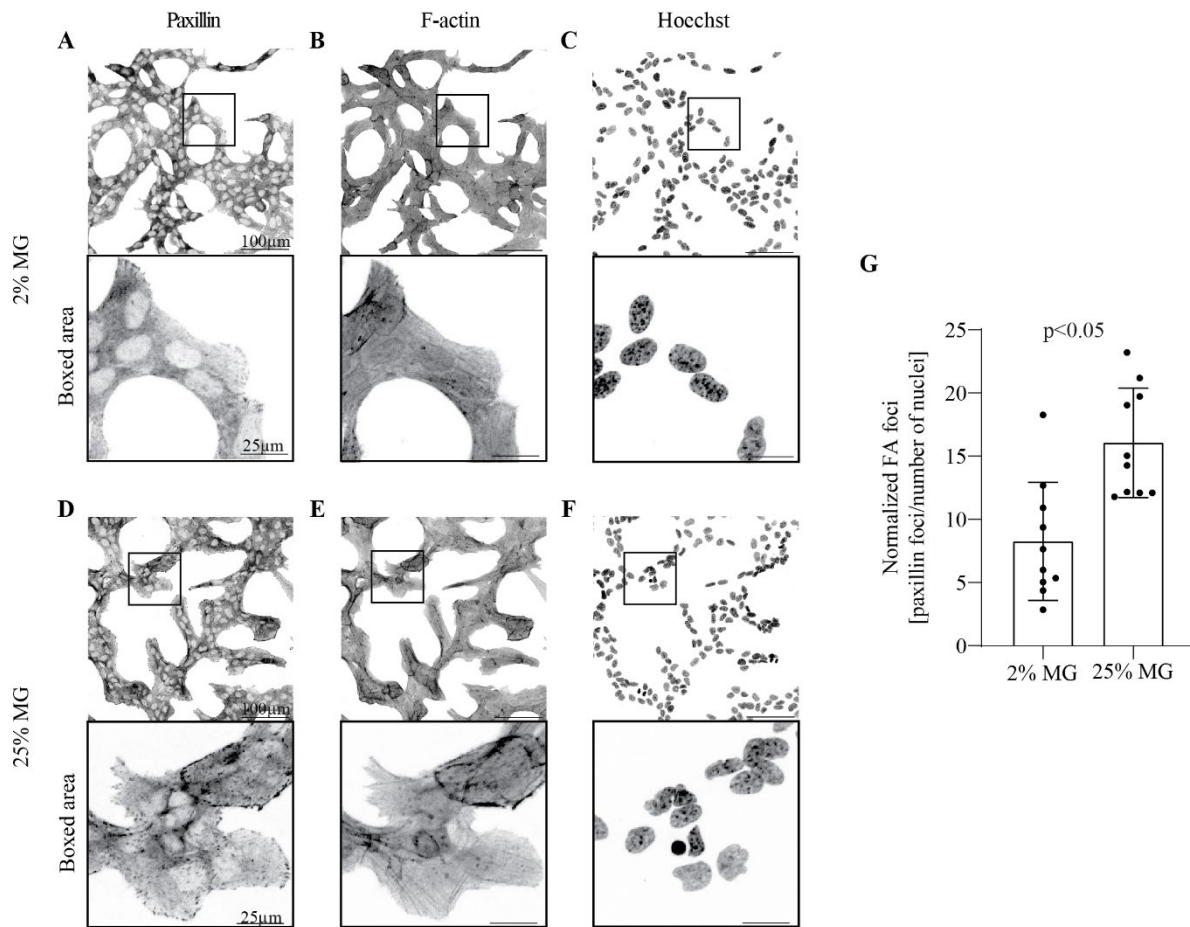
FNE-m-p53

S. Figure 6. Evaluation of focal adhesions in FNE-mp53 cells overlayed with 2% or 25% MG. (**A**) Adhered monolayer of FNE-m-p53 cells was overlayed with (**A, B, C**) 2% or (**D, E, F**) 25% MG for 72 hours, fixed and stained by immunofluorescence with (**A, D**) antibodies against paxillin, (**B, E**) phalloidin-FITC (binding to F-actin), and (**C, F**) Hoechst 33342. (**G**) Quantification of the number of focal adhesions observed in FNE-m-p53 cells overlayed with 2% or 25% MG, respectively. Each data point corresponds to one field of view (FOV) containing (31-376 cells), with a total of 10 FOVs/ condition (2% & 25%). All data points are shown with bars indicating mean ± SD. An unpaired, two-tailed, parametric student t-test with Welch's correction was used to examine statistical differences between data sets. Y-axis represents the number of paxillin foci normalized to the number of nuclei per ROI.

864
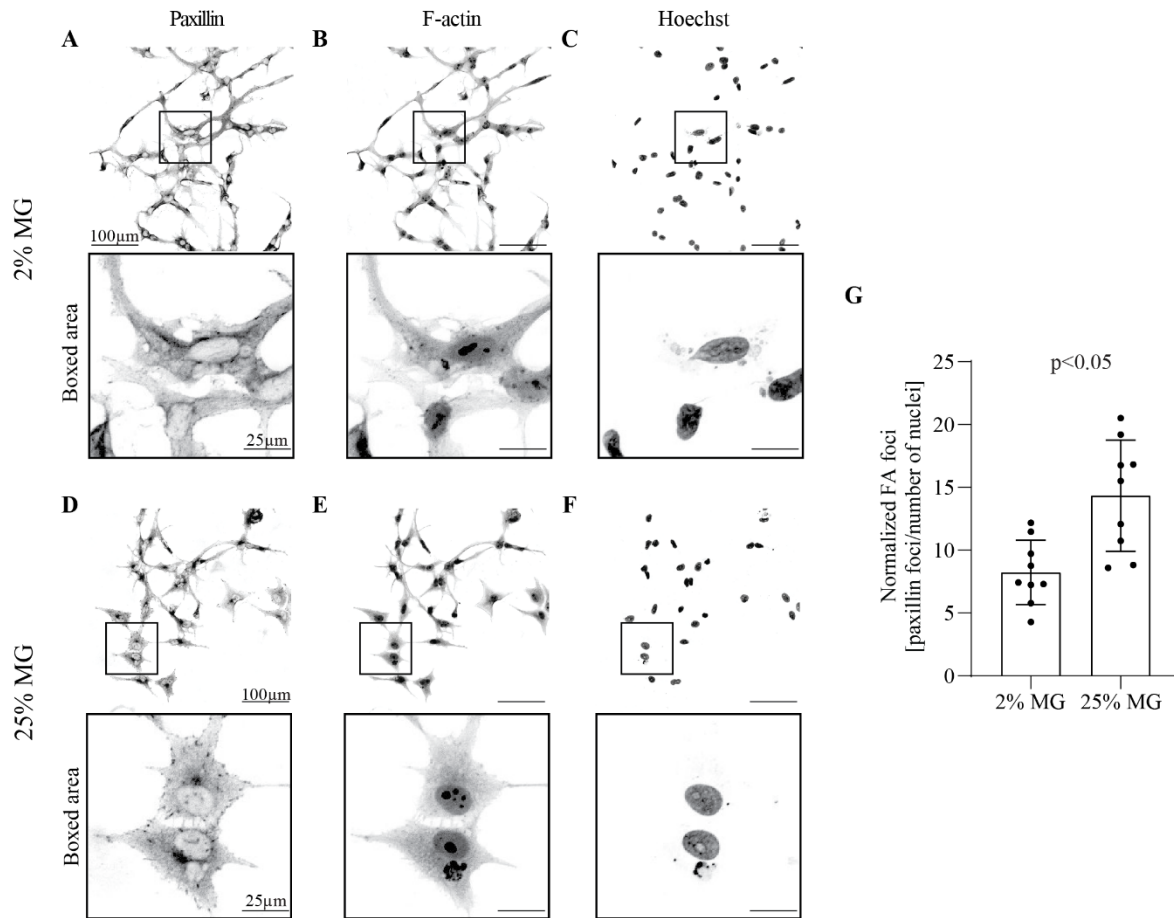
S. Figure 7. Evaluation of focal adhesions Hey-A8 monolayers overlayed with 2% or 25% MG. (**A**) Adhered monolayer of Hey-A8 cells was overlayed with (**A, B, C**) 2% or (**D, E, F**) 25% MG for 72 hours, fixed, and stained by immunofluorescence with (**A, D**) antibodies against paxillin, (**B, E**) phalloidin-FITC (binding to F-actin), and (**C, F**) Hoechst 33342. (**G**) Quantification of the number of focal adhesions observed in Hey-A8 cells overlayed with 2% or 25% MG, respectively. Each data point is one ROI (12-149 cells). All data points are shown with bars indicating mean ± SD. An unpaired, two-tailed, parametric student t-test with Welch's correction was used to examine statistical differences between data sets. Y-axis represents the number of paxillin foci normalized to the number of nuclei per ROI.
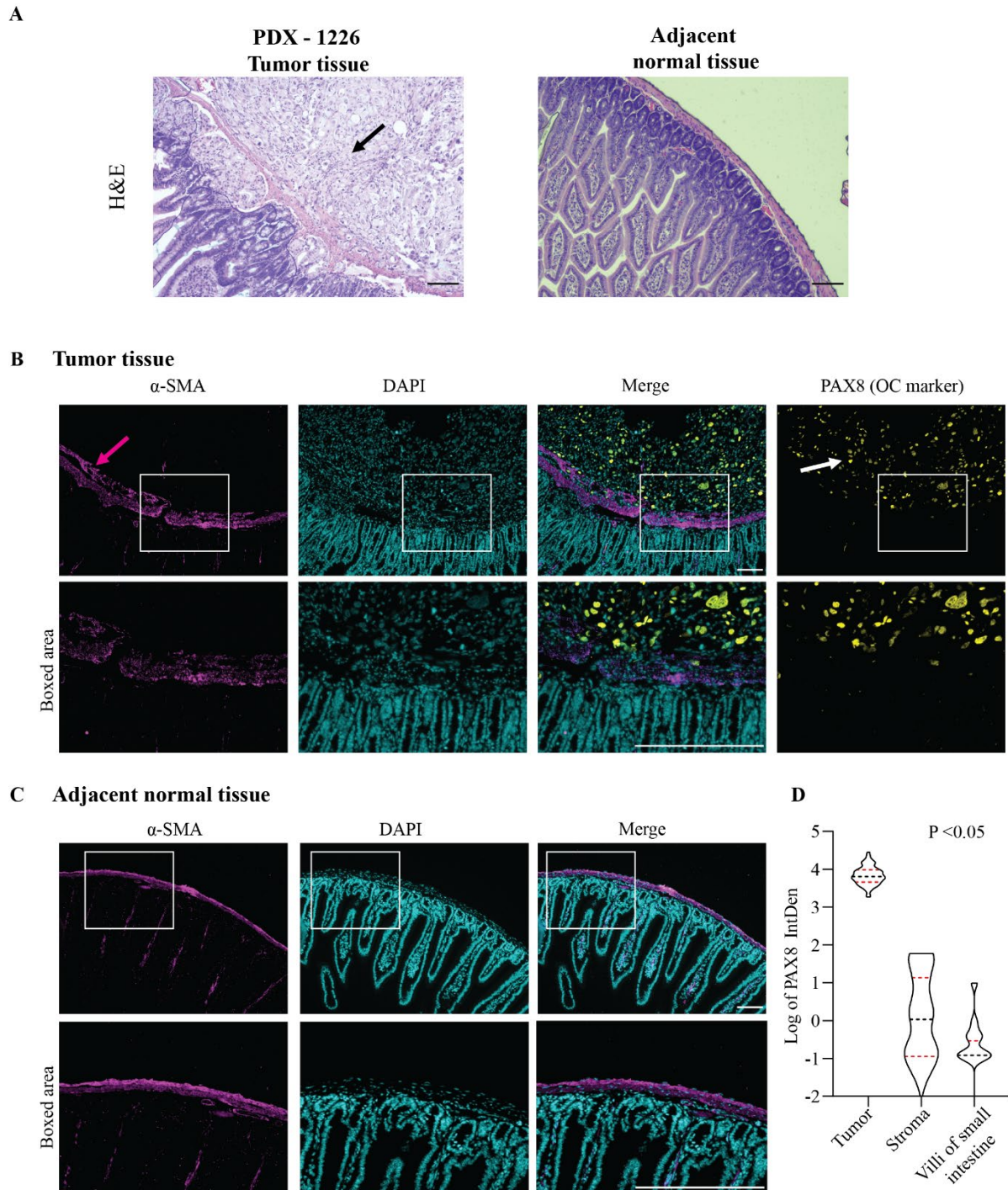
S. Figure 8. PDX-1226 growing tumor on the surface of the small intestine. (**A**) H&E of tumor nests (black arrow) and adjacent normal tissues. (**B**) Immunofluorescence of alpha smooth muscle actin (α-SMA) (magenta arrows), DAPI, PAX8 (white arrows) in tumor section. (**C**) Immunofluorescence of α-SMA and DAPI in adjacent normal tissue. Scale bars are 100 μm. (**D**) Quantification of PAX8 fluorescence intensity (integrated density). Each data point represents one region of interest (ROI). Total ROIs: tumor 66, stroma 20, and villi 20. All data points are shown as median and quartiles. An ordinary one-way ANOVA test was used to examine statistical differences between data sets. ANOVA was followed by Tukey post-hoc analysis; Tumor vs. Stroma P < 0.001, Tumor vs. Villi small intestine P < 0.001, Stroma vs. Villi small intestine P > 0.999.

Supplementary Movies.

MOVIE 1. Outgrowth formation by FNE-m-p53 spheroids reconstituted with 2% MG. Cell clusters were imaged for 5 days at 2-hr intervals.

MOVIE 2. Outgrowth formation by Hey-A8 spheroids reconstituted with 2% MG. Cell clusters were imaged for 5 days at 2-hr intervals.

MOVIE 3. Outgrowth formation by Tyk-nu spheroids reconstituted with 2% MG. Cell clusters were imaged for 5 days at 2-hr intervals.

MOVIE 4. FNE-m-p53-GFP cell proliferation in 2% and 25% MG. Images were obtained every 22 minutes for a duration of 61 hrs.

MOVIE 5. Hey-A8-mKO2 cell proliferation in 2% and 25% MG. Images were obtained every 22 minutes for a duration of 68 hrs.

MOVIE 6. Evolution of trajectories made by FNE-m-p53-GFP monolayer cultures overlayed with 2% or 25% MG. Images were obtained every 20 minutes for a duration of 61 hours. First frame of the movie corresponds to 13-hour time point.

MOVIE 7. Evolution of cell movement trajectories in Hey-A8-mKO2 monolayer cultures overlayed with 2% or 25% MG. Images were obtained every 15 minutes for a duration of 68 hours. First frame of the movie corresponds to 20-hour time point.

References

1.   Kurman RJ, Shih IM. The origin and pathogenesis of epithelial ovarian cancer: a proposed unifying theory. Am J Surg Pathol [Internet] 2010 [cited 2022 Apr 16];34(3):433–43. Available from: https://pubmed.ncbi.nlm.nih.gov/20154587/

2.   Auersperg N. Ovarian surface epithelium as a source of ovarian cancers: unwarranted speculation or evidence-based hypothesis? Gynecol Oncol [Internet] 2013 [cited 2022 Apr 16];130(1):246–51. Available from: https://pubmed.ncbi.nlm.nih.gov/23558054/

3.   Folkins AK, Jarboe EA, Saleemuddin A, Lee Y, Callahan MJ, Drapkin R, et al. A candidate precursor to pelvic serous cancer (p53 signature) and its prevalence in ovaries and fallopian tubes from women with BRCA mutations. Gynecol Oncol [Internet] 2008 [cited 2022 Apr 16];109(2):168–73. Available from: https://pubmed.ncbi.nlm.nih.gov/18342932/

910 4.   Meserve EEK, Brouwer J, Crum CP. Serous tubal intraepithelial neoplasia: the concept and its
911   application. Mod Pathol [Internet] 2017 [cited 2022 Apr 16];30(5):710–21. Available from:
912   https://pubmed.ncbi.nlm.nih.gov/28106106/

913 5.   Karst AM, Drapkin R. Ovarian cancer pathogenesis: a model in evolution. J Oncol [Internet]
914   2010   [cited   2022   Apr   16];2010:1–13.   Available   from:
915   https://pubmed.ncbi.nlm.nih.gov/19746182/

916 6.   Lengyel E. Ovarian cancer development and metastasis. Am J Pathol [Internet] 2010 [cited 2022
917   Apr 16];177(3):1053–64. Available from: https://pubmed.ncbi.nlm.nih.gov/20651229/

918 7.   Ahmed N, Stenvers KL. Getting to know ovarian cancer ascites: opportunities for targeted
919   therapy-based translational research. Front Oncol [Internet] 2013 [cited 2022 Apr 16];3.
920   Available from: https://pubmed.ncbi.nlm.nih.gov/24093089/

921 8.   Iwanicki MP, Chen HY, Iavarone C, Zervantonakis IK, Muranen T, Novak M, et al. Mutant p53
922   regulates ovarian cancer transformed phenotypes through autocrine matrix deposition. JCI
923   Insight   [Internet]   2016   [cited   2022   Apr   16];1(10):86829.   Available   from:
924   /pmc/articles/PMC4963159/

925 9.   Li X, Qian H, Takizawa M, Koga H, Tsuchisaka A, Ishii N, et al. N-linked glycosylation on
926   laminin γ1 influences recognition of anti-laminin γ1 pemphigoid autoantibodies. Journal of
927   Dermatological Science [Internet] 2015 [cited 2022 Apr 16];77(2):125–9. Available from:
928   http://www.jdsjournal.com/article/S0923181114003016/fulltext

929 10. Hennet T. Collagen glycosylation. Current Opinion in Structural Biology 2019;56:131–8.

930 11. Chen D, Roberts R, Pohl M, Nigam S, Kreidberg J, Wang Z, et al. Differential expression of
931   collagen- and laminin-binding integrins mediates ureteric bud and inner medullary collecting
932   duct cell tubulogenesis. American Journal of Physiology - Renal Physiology [Internet] 2004
933   [cited   2022   Apr   16];287(4   56-4):602–11.   Available   from:
934   https://journals.physiology.org/doi/full/10.1152/ajprenal.00015.2004

935 12. Chen CS, Tan J, Tien J. Mechanotransduction at Cell-Matrix and Cell-Cell Contacts.
936   http://dx.doi.org/101146/annurev.bioeng6040803140040 [Internet] 2004 [cited 2022 Apr
937   16];6:275–302.   Available   from:
938   https://www.annualreviews.org/doi/abs/10.1146/annurev.bioeng.6.040803.140040

939 13. Orr AW, Helmke BP, Blackman BR, Schwartz MA. Mechanisms of mechanotransduction. Dev
940   Cell   [Internet]   2006   [cited   2022   Apr   16];10(1):11–20.   Available   from:
941   https://pubmed.ncbi.nlm.nih.gov/16399074/

942 14. Wang C, Brisson BK, Terajima M, Li Q, Hoxha K, Han B, et al. Type III collagen is a key
943   regulator of the collagen fibrillar structure and biomechanics of articular cartilage and meniscus.
944   Matrix Biology 2020;85–86:47–67.

15. Spofford CM, Chilian WM. Mechanotransduction via the elastin-laminin receptor (ELR) in resistance arteries. J Biomech [Internet] 2003 [cited 2022 Apr 16];36(5):645–52. Available from: https://pubmed.ncbi.nlm.nih.gov/12694994/

16. Banno A, Ginsberg MH. Integrin activation. Biochemical Society Transactions [Internet] 2008 [cited 2022 Apr 16];36(2):229–34. Available from: /biochemsoctrans/article/36/2/229/83770/Integrin-activation

17. Schwartz MA, Shattil SJ. Signaling networks linking integrins and Rho family GTPases. Trends in Biochemical Sciences 2000;25(8):388–91.

18. Fields B, DeLaForest A, Zogg M, May J, Hagen C, Komnick K, et al. The Adult Murine Intestine is Dependent on Constitutive Laminin-γ1 Synthesis. Scientific Reports 2019 9:1 [Internet] 2019 [cited 2022 Apr 16];9(1):1–12. Available from: https://www.nature.com/articles/s41598-019-55844-x

19. Willem M, Miosge N, Halfter W, Smyth N, Jannetti I, Burghart E, et al. Specific ablation of the nidogen-binding site in the laminin γ1 chain interferes with kidney and lung development. Development [Internet] 2002 [cited 2022 Apr 16];129(11):2711–22. Available from: https://journals.biologists.com/dev/article/129/11/2711/41683/Specific-ablation-of-the-nidogen-binding-site-in

20. Jailkhani N, Ingram JR, Rashidian M, Rickelt S, Tian C, Mak H, et al. Noninvasive imaging of tumor progression, metastasis, and fibrosis using a nanobody targeting the extracellular matrix. Proc Natl Acad Sci U S A 2019;116(28):14181–90.

21. Winkler J, Abisoye-Ogunniyan A, Metcalf KJ, Werb Z. Concepts of extracellular matrix remodelling in tumour progression and metastasis. Nature Communications 2020 11:1 [Internet] 2020 [cited 2022 Apr 16];11(1):1–19. Available from: https://www.nature.com/articles/s41467-020-18794-x

22. Kuhn E, Kurman RJ, Soslow RA, Han G, Sehdev AS, Morin PJ, et al. The diagnostic and biological implications of laminin expression in serous tubal intraepithelial carcinoma. Am J Surg Pathol [Internet] 2012 [cited 2022 Apr 16];36(12):1826. Available from: /pmc/articles/PMC3500426/

23. Rentchler EC, Gant KL, Drapkin R, Patankar M, Campagnola PJ. Imaging Collagen Alterations in STICs and High Grade Ovarian Cancers in the Fallopian Tubes by Second Harmonic Generation Microscopy. Cancers 2019, Vol 11, Page 1805 [Internet] 2019 [cited 2022 Apr 16];11(11):1805. Available from: https://www.mdpi.com/2072-6694/11/11/1805/htm

24. Benton G, Arnaoutova I, George J, Kleinman HK, Koblinski J. Matrigel: From discovery and ECM mimicry to assays and models for cancer research. Advanced Drug Delivery Reviews 2014;79–80:3–18.

25. Mroue R, Bissell MJ. Three-Dimensional Cultures of Mouse Mammary Epithelial Cells. Methods in Molecular Biology [Internet] 2012 [cited 2022 Apr 16];945:221–50. Available from: https://link.springer.com/protocol/10.1007/978-1-62703-125-7_14

26. Farsinejad S, Cattabiani T, Muranen T, Iwanicki M. Ovarian Cancer Dissemination—A Cell Biologist's Perspective. Cancers 2019, Vol 11, Page 1957 [Internet] 2019 [cited 2022 Apr 16];11(12):1957. Available from: https://www.mdpi.com/2072-6694/11/12/1957/htm

27. Muranen T, Selfors LM, Worster DT, Iwanicki MP, Song L, Morales FC, et al. Inhibition of PI3K/mTOR Leads to Adaptive Resistance in Matrix-Attached Cancer Cells. Cancer Cell 2012;21(2):227–39.

28. Zhang S, Dolgalev I, Zhang T, Ran H, Levine DA, Neel BG. Both fallopian tube and ovarian surface epithelium are cells-of-origin for high-grade serous ovarian carcinoma. Nature Communications 2019 10:1 [Internet] 2019 [cited 2022 Apr 16];10(1):1–16. Available from: https://www.nature.com/articles/s41467-019-13116-2

29. Zhang S, Iyer S, Ran H, Dolgalev I, Gu S, Wei W, et al. Genetically defined, syngeneic organoid platform for developing combination therapies for ovarian cancer. Cancer Discovery [Internet] 2021 [cited 2022 Apr 16];11(2):362–83. Available from: https://aacrjournals.org/cancerdiscovery/article/11/2/362/3255/Genetically-Defined-Syngeneic-Organoid-Platform

30. Hill SJ, Decker B, Roberts EA, Horowitz NS, Muto MG, Worley MJ, et al. Prediction of DNA repair inhibitor response in short-term patient-derived ovarian cancer organoids. AACR [Internet] [cited 2022 Apr 16];Available from: https://cancerdiscovery.aacrjournals.org/content/8/11/1404.abstract

31. Hoffmann K, Berger H, Kulbe H, Thillainadarasan S, Mollenkopf H, Zemojtel T, et al. Stable expansion of high-grade serous ovarian cancer organoids requires a low-Wnt environment. The EMBO Journal 2020;39(6).

32. McPherson A, Roth A, Laks E, Masud T, Bashashati A, Zhang AW, et al. Divergent modes of clonal spread and intraperitoneal mixing in high-grade serous ovarian cancer. Nat Genet [Internet] 2016 [cited 2022 Jun 29];48(7):758–67. Available from: https://pubmed.ncbi.nlm.nih.gov/27182968/

33. Lee YY, Kim YJ, Gil ES, Kim H, Jang JH, Choung YH. Type 1 Diabetes Induces Hearing Loss: Functional and Histological Findings in An Akita Mouse Model. Biomedicines 2020, Vol 8, Page 343 [Internet] 2020 [cited 2022 Feb 26];8(9):343. Available from: https://www.mdpi.com/2227-9059/8/9/343/htm

34. Wegner K, … AK… of H&, 2017 undefined. Fluorescence of picrosirius red multiplexed with immunohistochemistry for the quantitative assessment of collagen in tissue sections. journals.sagepub.com [Internet] 2017 [cited 2022 Apr 16];65(8):479–90. Available from: https://journals.sagepub.com/doi/abs/10.1369/0022155417718541

35. Kleinman HK, McGarvey ML, Hassell JR, Star VL, Cannon FB, Laurie GW, et al. Basement membrane complexes with biological activity. Biochemistry [Internet] 1986 [cited 2022 Apr 16];25(2):312–8. Available from: https://pubmed.ncbi.nlm.nih.gov/2937447/

36. Martin GR, Timpl R, Kühn K. Basement membrane proteins: molecular structure and function. Adv Protein Chem [Internet] 1988 [cited 2022 Apr 16];39(C):1–50. Available from: https://pubmed.ncbi.nlm.nih.gov/3149870/

37. Aisenbrey EA, Murphy WL. Synthetic alternatives to Matrigel. Nature Reviews Materials 2020 5:7 [Internet] 2020 [cited 2022 Apr 16];5(7):539–51. Available from: https://www.nature.com/articles/s41578-020-0199-8

38. Domcke S, Sinha R, Levine DA, Sander C, Schultz N. Evaluating cell lines as tumour models by comparison of genomic profiles. Nat Commun [Internet] 2013 [cited 2022 Apr 16];4. Available from: https://pubmed.ncbi.nlm.nih.gov/23839242/

39. Davidowitz RA, Iwanicki MP, Brugge JS. In vitro Mesothelial Clearance Assay that Models the Early Steps of Ovarian Cancer Metastasis. Journal of Visualized Experiments : JoVE [Internet] 2012 [cited 2022 Jun 23];(60):3888. Available from: /pmc/articles/PMC3466628/

40. Iwanicki MP, Davidowitz RA, Ng MR, Besser A, Muranen T, Merritt M, et al. Ovarian cancer spheroids use myosin-generated force to clear the mesothelium. Cancer Discovery [Internet] 2011 [cited 2022 Apr 16];1(2):144–57. Available from: https://aacrjournals.org/cancerdiscovery/article/1/2/144/2263/Ovarian-Cancer-Spheroids-Use-Myosin-Generated

41. LeCluyse EL, Bullock PL, Parkinson A, Hochman JH. Cultured rat hepatocytes. Pharm Biotechnol 1996;8:121–59.

42. Borries M, Barooji YF, Yennek S, Grapin-Botton A, Berg-Sørensen K, Oddershede LB. Quantification of Visco-Elastic Properties of a Matrigel for Organoid Development as a Function of Polymer Concentration. Frontiers in Physics 2020;8:475.

43. Barriga E, Biology RMS in C& D, 2019 undefined. Adjustable viscoelasticity allows for efficient collective cell migration. Elsevier [Internet] [cited 2022 Apr 16];Available from: https://www.sciencedirect.com/science/article/pii/S1084952117305505

44. migration MAC adhesion &, 2013 undefined. The laminin family. Taylor & Francis [Internet] 2013 [cited 2022 Apr 16];7(1):48–55. Available from: https://www.tandfonline.com/doi/abs/10.4161/cam.22826

45. in PYCSH perspectives, 2011 undefined. Basement membranes: cell scaffoldings and signaling platforms. cshperspectives.cshlp.org [Internet] [cited 2022 Apr 16];Available from: https://cshperspectives.cshlp.org/content/3/2/a004911.short

46. Kyprianou C, Christodoulou N, Nature RH, 2020 undefined. Basement membrane remodelling regulates mouse embryogenesis. nature.com [Internet] [cited 2022 Apr 16];Available from: https://idp.nature.com/authorize/casa?redirect_uri=https://www.nature.com/articles/s41586-

1054 020-2264-2&casa_token=KJ1B8x3SFB0AAAAA:f3sEXt-R5JzjnY2l-

1055 R_brrEC4otGF3VzFdVumgZ4qkEaT_CPZP8dDZI01p3JfuWudLgZ1V-m32vfOPPd

1056 47. Delaine-Smith R, Maniati E, Malacrida B, iScience SN, 2021 undefined. Modelling TGFβR and

1057 Hh pathway regulation of prognostic matrisome molecules in ovarian cancer. Elsevier [Internet]

1058 [cited   2022   Apr   16];Available   from:

1059 https://www.sciencedirect.com/science/article/pii/S2589004221006428

1060 48. Raspanti M, Viola M, Sonaggere M, Tira ME, Tenni R. Collagen fibril structure is affected by

1061 collagen concentration and decorin. Biomacromolecules 2007;8(7):2087–91.

1062 49. Fraley SI, Wu PH, He L, Feng Y, Krisnamurthy R, Longmore GD, et al. Three-dimensional

1063 matrix fiber alignment modulates cell migration and MT1-MMP utility by spatially and

1064 temporally directing protrusions. Sci Rep [Internet] 2015 [cited 2022 Jun 30];5. Available from:

1065 https://pubmed.ncbi.nlm.nih.gov/26423227/

1066 50. Hsu YM, Chen CN, Chiu JJ, Chang SH, Wang YJ. The effects of fiber size on MG63 cells

1067 cultured with collagen based matrices. J Biomed Mater Res B Appl Biomater [Internet] 2009

1068 [cited 2022 Jun 30];91(2):737–45. Available from: https://pubmed.ncbi.nlm.nih.gov/19572296/

1069 51. Jana A, Nookaew I, Singh J, Behkam B, Franco AT, Nain AS. Crosshatch nanofiber networks

1070 of tunable interfiber spacing induce plasticity in cell migration and cytoskeletal response.

1071 FASEB J [Internet] 2019 [cited 2022 Jun 29];33(10):10618–32. Available from:

1072 https://pubmed.ncbi.nlm.nih.gov/31225977/

1073 52. Plou J, Juste-Lanas Y, Olivares V, del Amo C, Borau C, García-Aznar JM. From individual to

1074 collective 3D cancer dissemination: roles of collagen concentration and TGF-β. Scientific

1075 Reports 2018 8:1 [Internet] 2018 [cited 2022 Apr 16];8(1):1–14. Available from:

1076 https://www.nature.com/articles/s41598-018-30683-4

1077 53. Palecek SP, Loftust JC, Ginsbergt MH, Lauffenburger DA, Horwitz AF. Integrin-ligand binding

1078 properties govern cell migration speed through cell-substratum adhesiveness. nature.com

1079 [Internet] 1997 [cited 2022 Apr 16];385:3–4. Available from:

1080 https://idp.nature.com/authorize/casa?redirect_uri=https://www.nature.com/articles/385537a0

1081 &casa_token=QdaKLV0-wYMAAAAA:-zD_b-

1082 jDXRhWSxrg_emp9Xbz4bie6fCYxwlxGhfAof17yWSxJ7P-

1083 AbNylrH1lFkq3_1YJgtbWjAKpQeh

1084 54. Webb D, Parsons J, biology AHN cell, 2002 undefined. Adhesion assembly, disassembly and

1085 turnover in migrating cells–over and over and over again. nature.com [Internet] [cited 2022 Apr

1086 16];Available   from:

1087 https://idp.nature.com/authorize/casa?redirect_uri=https://www.nature.com/articles/ncb0402-

1088 e97&casa_token=pa9fRR9BiQQAAAAA:Gz9cG7n0gv7gkC8_nvIqr2H5YIIKKVaiVXXQ6iy

1089 aHwS6KqLIAHDNzgHc-cCmUPX9eJEkouRHzyRqXQEE

1090   55.   Chaudhuri O, Cooper-White J, Janmey P, Nature DM, 2020 undefined. Effects of extracellular
1091   matrix viscoelasticity on cellular behaviour. nature.com [Internet] [cited 2022 Apr 16];Available
1092   from:
1093   https://idp.nature.com/authorize/casa?redirect_uri=https://www.nature.com/articles/s41586-
1094   020-2612-2&casa_token=LV6_Z_5X_HYAAAAA:NGvuLkWvRaBl-
1095   3DycCu9ngnlNkM_3BO3bqsoTQiAibF2B6UUZLQbaXsN-jJfW3UX-717VCKZELv9N9Ny

1096   56.   Chaudhuri O, Koshy ST, Branco Da Cunha C, Shin JW, Verbeke CS, Allison KH, et al.
1097   Extracellular matrix stiffness and composition jointly regulate the induction of malignant
1098   phenotypes in mammary epithelium. Nat Mater [Internet] 2014 [cited 2022 Apr 16];13(10):970–
1099   8. Available from: https://pubmed.ncbi.nlm.nih.gov/24930031/

1100   57.   Byers L, Osborne J, Carson L, Carter J, letters AHC, 1995 undefined. Increased levels of laminin
1101   in ascitic fluid of patients with ovarian cancer. Elsevier [Internet] [cited 2022 Apr 16];Available
1102   from: https://www.sciencedirect.com/science/article/pii/030438359403625S

1103   58.   Maniati E, Berlato C, Gopinathan G, Heath O, Kotantaki P, Lakhani A, et al. Mouse Ovarian
1104   Cancer Models Recapitulate the Human Tumor Microenvironment and Patient Response to
1105   Treatment. Cell Rep [Internet] 2020 [cited 2022 Jun 30];30(2):525-540.e7. Available from:
1106   https://pubmed.ncbi.nlm.nih.gov/31940494/

1107   59.   Ince TA, Richardson AL, Bell GW, Saitoh M, Godar S, Karnoub AE, et al. Transformation of
1108   different human breast epithelial cell types leads to distinct tumor phenotypes. Cancer Cell
1109   [Internet]   2007   [cited   2022   Jun   23];12(2):160–70.   Available   from:
1110   https://pubmed.ncbi.nlm.nih.gov/17692807/

1111   60.   Uphoff CC, Drexler HG. Detection of Mycoplasma Contaminations. Methods in Molecular
1112   Biology   [Internet]   2013   [cited   2022   Apr   16];946:1–13.   Available   from:
1113   https://link.springer.com/protocol/10.1007/978-1-62703-128-8_1

1114   61.   Lee Y, Kim Y, Gil E, Kim H, Jang J, Biomedicines YC, et al. Type 1 Diabetes Induces Hearing
1115   Loss: Functional and Histological Findings in An Akita Mouse Model. mdpi.com [Internet]
1116   [cited 2022 Apr 16];Available from: https://www.mdpi.com/823960

1117   62.   Schindelin J, Arganda-Carreras I, Frise E, … VKN, 2012 undefined. Fiji: an open-source
1118   platform for biological-image analysis. nature.com [Internet] [cited 2022 Apr 16];Available
1119   from: https://www.nature.com/articles/nmeth.2019

1120   63.   Wang S, Liu CH, Zakharov VP, Lazar AJ, Pollock RE, Larin K v. Three-dimensional
1121   computational analysis of optical coherence tomography images for the detection of soft tissue
1122   sarcomas. spiedigitallibrary.org [Internet] 2014 [cited 2022 Apr 16];19(2):021102. Available
1123   from: https://www.spiedigitallibrary.org/journals/journal-of-biomedical-optics/volume-
1124   19/issue-2/021102/Three-dimensional-computational-analysis-of-optical-coherence-
1125   tomography-images-for/10.1117/1.JBO.19.2.021102.short

1126   64.   Tinevez J, Perry N, Schindelin J, Methods GH, 2017 undefined. TrackMate: An open and
1127   extensible platform for single-particle tracking. Elsevier [Internet] [cited 2022 Apr
1128   16];Available from: https://www.sciencedirect.com/science/article/pii/S1046202316303346
1129   65.   Wagner T, Kroll A, Haramagatti CR, Lipinski HG, Wiemann M. Classification and
1130   segmentation of nanoparticle diffusion trajectories in cellular micro environments. PLoS ONE
1131   2017;12(1).